GENG5512 MPE Engineering Research Project Part 2

Final Report

Electric Hydrofoil Jet ski

Timothy Fleay
23077735
School of Engineering, University of Western Australia

Supervisor: Thomas Braunl
School of Engineering, University of Western Australia

Word count: 7,995

School of Engineering
University of Western Australia

Submitted: 20 May 2026

Project Summary
The global transition toward low-emission transport has created a compelling case for the electrification of marine recreation, a sector where significant efficiency gains remain largely unrealised. Conventional personal watercraft produce considerable emissions, noise, and wake, yet cleaner alternatives remain largely undemonstrated at prototype scale in Australia. UWA and Oceanomatics have identified this gap, with the current prototype requiring resolution of several outstanding mechanical challenges before operational trials can proceed.

This project addresses key mechanical engineering requirements of UWA's electric hydrofoil jet ski, contributing to the progression of the prototype through the design, analysis, and fabrication of three critical subsystems. The first objective is the design and fabrication of a structural chassis base plate capable of safely supporting the battery and foil assemblies under all anticipated operational loading conditions. The second objective is the development of a waterproofing enclosure for the battery system, ensuring all enclosed electrical components are protected against saltwater ingress, and safeguarding the reliability and longevity of the electrical systems. The third objective is the design and implementation of a water-cooling system for the outboard motor and an ESC, ensuring adequate thermal management is maintained throughout sustained operation.

Approaches to achieving these objectives followed a consistent methodology across all three subsystems. Design requirements and constraints were established to inform component selection and geometry, with all designs modelled in Fusion 360 and validated analytically prior to fabrication.

The chassis base plate was redesigned from an existing concept to resolve geometric interference within the hull envelope. FEA confirmed structural adequacy under all anticipated load cases, achieving a minimum factor of safety of 2.18. The acrylic battery enclosure was fabricated and subjected to IP65 hose testing; an initial failure attributed to inconsistent solvent cement bonding was remediated through secondary silicone sealing, with subsequent testing confirming watertight integrity. Pressure relief analysis confirmed the selected breather vents provide a combined flow capacity substantially exceeding the calculated peak thermal expansion demand. For the water-cooling system, a dual-circuit architecture was adopted, a raw seawater loop for the motor and a closed freshwater loop for the ESC, resolving corrosion and thermal sequencing issues identified in the initial single-circuit concept. Analytical verification confirmed a predicted ESC temperature of 77.8°C at design operating conditions, satisfying the 85°C thermal limit with a 7.2°C margin.

Future work should prioritise leak testing and commissioning of the motor raw water circuit, full installation of the ESC closed-loop system including radiator mounting and hull penetration sealing, and operational water trials to validate thermal performance against analytical predictions. CFD analysis is recommended to improve hydrodynamic load estimates for the base plate, and the acrylic enclosure bond line should be inspected and remediated prior to electrical integration to address the localised stress concentrations identified in the structural FEA.

Acknowledgements

The author would like to thank supervisor Professor Thomas Braunl and co-supervisor Pierre-Louis Francois Constant for their guidance and technical feedback throughout the project. Appreciation is also extended to PhD student Tiziano Wehrli and fellow project team members for their collaboration and support across the multidisciplinary aspects of the build. The Engineering Workshop staff, particularly John Hitchings, are acknowledged for their assistance during fabrication. Finally, the author is grateful to family and friends for their continued support throughout the year.

Nomenclature

A	Area
A_b	Battery surface area
A_{ac}	Acrylic wall surface area
A_{al}	Aluminium plate surface area
$A_{battery}$	Battery loading area
A_w	Wall surface area
c	Specific heat capacity
c_a	Specific heat capacity of air
c_{ac}	Specific heat capacity of acrylic
c_{al}	Specific heat capacity of aluminium
c_b	Specific heat capacity of battery
C_D	Drag coefficient
C_L	Lift coefficient
D	Drag force
F	Force

F_H	Horizontal force
$F_{horizontal}$	Horizontal hydrodynamic force
$F_{i,horizontal}$	Horizontal force at bolt location i
$F_{i,vertical}$	Vertical force at bolt location i
F_{lift}	Lift force
F_{rear}	Rear foil reaction force
F_{thrust}	Thrust force
F_V	Vertical force
$F_{v,front,total}$	Total vertical force on front bolts
$F_{v,rear,total}$	Total vertical force on rear bolts
g	Acceleration due to gravity
h	Convective heat transfer coefficient
h_{aw}	Convective heat transfer coefficient between air and wall
h_{ba}	Convective heat transfer coefficient between battery and air
h_{wo}	External wall convective heat transfer coefficient
L	Lift force
m	Mass
m_a	Mass of air
m_{ac}	Mass of acrylic
m_{al}	Mass of aluminium
m_b	Mass of battery
P	Pressure
Q	Heat transfer rate
$\dot{Q}$	Heat generation rate
q_v	Minimum ventilation rate
R	Thermal resistance
t	Time
T	Temperature
T_a	Internal air temperature
T_b	Battery temperature

$T_{w,ac}$	Acrylic wall temperature
$T_{w,al}$	Aluminium plate temperature
T_{∞}	Ambient temperature
V	Velocity
$\dot{V}$	Volumetric flow rate
V_{air}	Internal air volume
ρ	Fluid density
σ	Stress
$\sigma_{battery}$	Battery pressure stress
σ_{y}	Yield strength
ρ	Density
ω	Angular velocity

Abbreviations and Acronyms

CAD	Computer-Aided Design
CFD	Computational Fluid Dynamics
ESC	Electronic Speed Controller
FEA	Finite Element Analysis
IEC	International Electrotechnical Commission
IP	Ingress Protection
MOSFET	Metal-Oxide-Semiconductor Field-Effect Transistor
NMC	Nickel Manganese Cobalt
PMMA	Polymethyl Methacrylate
P&ID	Piping and Instrumentation Diagram
UWA	University of Western Australia
VESC	Vedder Electronic Speed Controller

1. Introduction

The global transition toward low-emission transport has created increasing pressure to electrify sectors beyond road vehicles, including marine recreation (CSIRO, 2026). Conventional personal watercraft operate as displacement hulls, consuming substantial propulsive power while producing considerable emissions, wake, and noise pollution (Erbe, 2013), yet cleaner alternatives remain largely undemonstrated at a commercial scale (Ricardo, 2025).

Hydrofoil technology offers a compelling response to this challenge. By lifting the hull above the waterline on submerged foils, hydrodynamic drag is dramatically reduced, enabling operation at a fraction of the propulsive power required by conventional hulls (Suh et al., 2021). Combined with electric propulsion, the result is a system producing zero direct emissions, minimal wake, and reduced noise (Candela, 2023). Despite these advantages, the integration of hydrofoil technology with electric propulsion in personal watercraft remains confined to early-stage products, with no solution demonstrated at scale for recreational use by unskilled operators (Ricardo, 2025).

UWA's electric hydrofoil jet ski addresses this gap directly and is among the first prototypes of its kind in Australia (Submersible Motor Engineering, 2016). Developed through a collaborative multidisciplinary effort spanning mechanical, electrical, and software engineering, the project is supported by Oceanomatics Pty Ltd, whose commercial interest in scalable production provides both industry context and motivation for the engineering outcomes of this work. A full system CAD assembly of this prototype is demonstrated by Figure 1.1

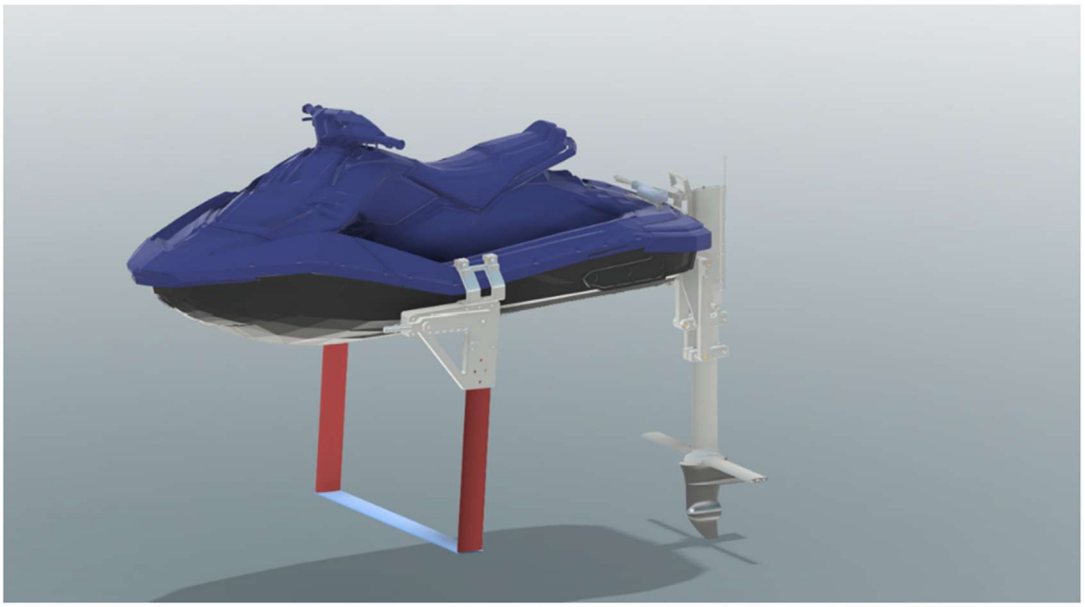

Figure 1.1: CAD assembly of the UWA electric hydrofoil jet ski

The mechanical scope encompasses chassis integration, waterproofing of all electrical components, front and rear hydrofoil design, water cooling, and bilge management. This report focuses specifically on the design and fabrication of the chassis base plate and battery waterproofing enclosure, and the implementation of a water-cooling system for the outboard motor and ESC. The mechanical scope and allocation of report coverage are summarised in Figure 1.2.

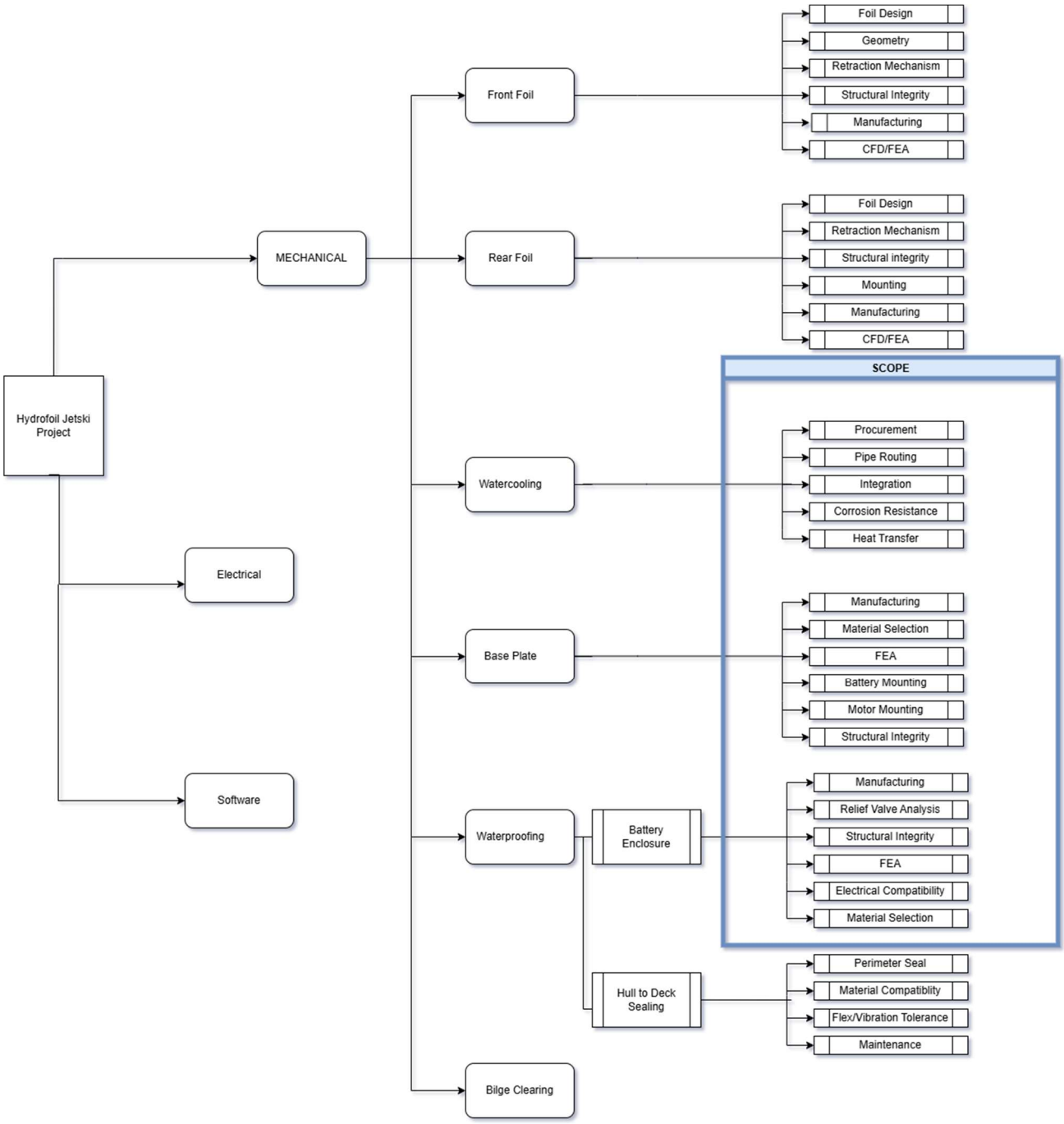

Figure 1.2: Functional breakdown structure of the hydrofoil jetski project

2. Literature Review

2.1 History and current state of the art of hydrofoil Jetski

Hydrofoil development spans over a century, beginning with Emmanuel Fargot's 1869 patent for a rowing craft with submerged lifting surfaces, and advancing through Enrico Forlanini's ladder foil designs, which achieved the first practical foil-borne runs on Lake Maggiore in 1906 (International Hydrofoil Society, n.d.). Through the early 20th century, Hans von Schertel's iterations established the foundational vocabulary of lift, immersion depth, and V-foil geometry, while post-war developments introduced active flight control, most notably Christopher Hook's feeler-float system and the US Navy's Boeing-designed USS High Point with electronically controlled fully submerged foils (Loibner, 2018). Navy hydrofoil patrol craft operated from 1977 to 1993 before being retired due to high maintenance costs (Federation of American Scientists, n.d.).

Today, the technology has matured into commercial transport and elite sport: the Candela P-12 Shuttle carries 30 passengers at 25 knots with 80% lower energy consumption than conventional ferries (Candela, 2024), the AC75 America's Cup yacht achieves 40 knots on canting foil arms (America’s Cup, 2024), and electric hydrofoil surfboards have emerged as a consumer personal mobility platform (Fliteboard, 2024).

Figure 2.1: Candela P-12 Shuttle operating in foil-borne mode, demonstrating commercial electric hydrofoil passenger transport (Candela, 2024).

2.2 Waterproofing of Marine Electrical System Literature

2.2.1 Battery Enclosure Design Approaches

Several approaches to battery enclosure waterproofing are documented in the literature. Metallic enclosures with rubber seals are dominant in EV applications but are poorly suited to custom low-volume fabrication due to high tooling costs (Liu et al., 2022). Fully integrated waterproof chassis

designs have been developed for marine use, though these are difficult to adapt to existing hull geometries (Fraunhofer ICT, 2021). Component-level alternatives, conformal coatings, encapsulation compounds, and heat shrink tubing, do not provide the system-level protection required for a battery assembly (Techspray, 2023).

The enclosure protection is governed by IEC 60529, which defines the two-digit IP rating system classifying resistance to solid and liquid ingress (International Electrotechnical Commission [IEC], 2013).

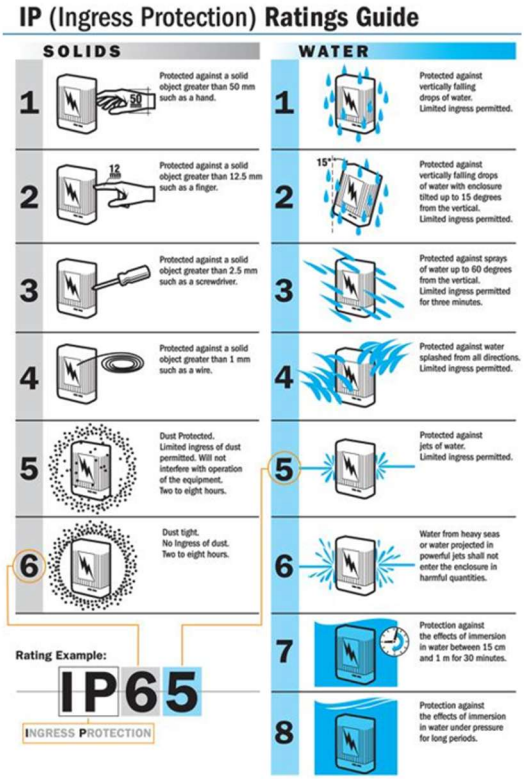

Figure 2.2: IP ingress protection rating classifications for solid particle and water resistance.

2.2.2 Acrylic Plastic and Polycarbonate Comparison

Both acrylic and polycarbonate are widely used transparent thermoplastics in marine enclosure applications (Curbell Plastics, 2024). Polycarbonate offers superior impact resistance, typically achieving an IK10 rating under IEC 62262 (International Electrotechnical Commission [IEC], 2002), making it preferred in high-impact environments. However, acrylic is favoured in offshore marine applications for its superior scratch resistance, UV durability, and lower cost (Acrylic Sheet Form, 2023). Critically, acrylic is uniquely compatible with solvent cement bonding, producing joints approaching parent material strength, an advantage polycarbonate does not offer (Trinseo, 2022).

2.3 Structural design of marine chassis components

The base plate operates in a demanding marine environment, subject to repeated hydrodynamic and vibrational loading throughout operation. Two material properties are therefore critical beyond static strength: fatigue performance under cyclic loading, and resistance to marine corrosion.

Carbon fibre composite offers the highest strength-to-weight ratio of candidate structural materials (Campbell, 2010), however its suitability in marine environments is significantly compromised by seawater exposure. Siriruk et al. demonstrated that immersion in seawater reduced the fatigue life of carbon fibre–vinyl ester composites by 80%, driven by matrix cracking and progressive fibre–matrix debonding (Siriruk et al., 2020). These degradation mechanisms are particularly problematic for a dynamically loaded structural component with no practical means of moisture exclusion at the material level, making carbon fibre unsuitable for this application despite its mechanical advantages in dry conditions

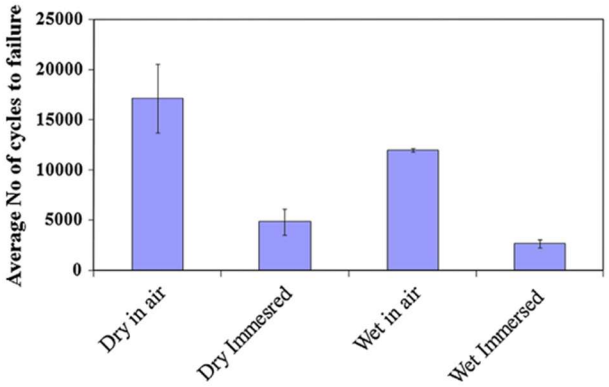

Figure 2.3: Average fatigue cycles to failure for acrylic bond specimens under dry and immersed conditions.

Stainless steel alloys offer good corrosion resistance and are widely used in marine structures; however, their high density (~7850–8000 kg/m³) results in a strength-to-weight ratio substantially lower than aluminium alternatives (Callister & Rethwisch, 2020), imposing unnecessary mass on a weight-sensitive vehicle.

Aluminium alloys in the 5000 series present a more suitable combination of properties for this application. They exhibit good marine corrosion resistance (The Aluminum Association, 2022), are readily weldable (Davis, 1993), and are available in sheet form compatible with waterjet cutting, a key manufacturability constraint for this project. Necemer et al. (Necemer et al., 2021) demonstrated that fatigue life in 5000 series aluminium is sensitive to loading orientation, with specimens loaded in the rolling direction exhibiting 25% greater fatigue life than transverse specimens under equivalent cyclic conditions. This finding informed the orientation of the base plate geometry relative to anticipated load paths. Taken together, the literature supports aluminium alloys in the 5000 series as the most appropriate material class for a welded marine structural plate subject to cyclic hydrodynamic loading.

2.4 Thermal management of electric marine propulsion

Heat generation in electric propulsion motors arises from copper losses in the stator windings, iron losses from hysteresis and eddy currents in the magnetic core, and mechanical friction losses (Pyrhönen et al., 2014). If not adequately managed, temperature rise degrades motor efficiency, accelerates insulation degradation, and can cause permanent demagnetisation of rotor magnets (Gieras, 2010). Gundabattini et al. (Gundabattini et al., 2020) reviewed a range of cooling

approaches for electric motors, finding that forced liquid cooling substantially outperforms air cooling due to the higher heat transfer capability of liquids under forced convection. Water jacket systems were reported to remove over 99.5% of generated heat, while advanced methods including nanofluids and heat pipes demonstrated further improvements, though these remain largely experimental.

3. Project Objectives

The global shift toward low-emission marine transport has created demand for electric personal watercraft capable of sustained high-performance operation (IEA, 2023). UWA's electric hydrofoil jet ski represents one of the first prototypes of its kind in Australia, developed in collaboration with Oceanomatics Pty Ltd. It is hypothesised that a structural base plate, acrylic waterproofing enclosure, and dual-circuit water-cooling system can be designed and validated to meet all defined performance requirements, advancing the prototype to a state ready for operational water trials.

The objectives of this project are:

- **O1:** Design and fabricate a structural chassis base plate capable of safely supporting the battery and foil assemblies under all anticipated operational loading conditions, with a minimum factor of safety of 2.0.
- **O2:** Design and fabricate a waterproofing enclosure for the battery system achieving a minimum IP65 ingress protection rating, ensuring electrical components are protected against saltwater ingress throughout operation.
- **O3:** Design and implement a water-cooling system for the outboard motor and ESC, maintaining motor winding temperature below 120°C and ESC junction temperature below 85°C during sustained operation.

This work advances the prototype toward operational water trials, enabling Oceanomatics to evaluate performance under recreational use conditions. Unresolved subsystem failures, particularly battery waterproofing, risk short-circuit, fire, and vessel loss with significant safety and financial consequences. Future students are expected to build on these foundations toward a fully operational prototype.

4. Design Approach

The design approach adopted across all three subsystems follows a consistent process. Requirements and constraints were established from each problem definition, informing material selection, component choice, and geometry, the requirements are design imposed targets while the constraints are fixed external conditions. Alternative concepts were generated and evaluated against these criteria, with selected designs modelled and validated through FEA in Autodesk Fusion 360 prior to fabrication. Where applicable, designs were verified against relevant Australian and international standards, and physical testing conducted to confirm performance against key requirements.

4.1 Battery Base Plate Process

4.1.1 Problem Definition

The battery base plate serves as the primary structural mounting platform for the vehicle's five NMC battery modules within the jet ski hull. Each module measures 355 mm × 151 mm × 108 mm and weighs approximately 11.6 kg (Shenzhen Tritek Limited, n.d.), requiring arrangement within the constrained internal hull geometry while maintaining accessibility for electrical connections and servicing. The plate interfaces with the hull via eight pre-existing bolt locations, four on each lateral side, with no hull modifications permissible. Structurally, the plate must resist bending induced by the distributed battery mass as well as forces transmitted through the front and rear foil attachment points. The marine environment introduces additional requirements for corrosion resistance and compatibility with the waterproofing enclosure system.

4.1.2 Design Requirements

The following design requirements, outlined in Table 4.1, were identified from the problem definition and form the basis for design decision-making and validation.

Table 4.1: Design requirements for the battery base plate

Requirement number	Requirement
R1,1	The base plate must support all realistic loading cases without yielding under static and dynamic loading conditions with a safety factor of 2.
R1,2	The plate must mount to the eight pre-existing hull bolt locations without modification to the hull structure.
R1,3	The plate must provide a sealed mounting interface for water proofing capabilities.
R1,4	The material must be corrosion resistant and suitable for a marine environment.
R1,5	Base plate must be weldable
R1,6	The base plate must incorporate a provision for front and rear foil attachment

4.1.3 Design Constraints

The battery base plate design is subject to a number of constraints imposed by the existing craft geometry and component specifications. These constraints are fixed external conditions that the design must accommodate and are summarised in Table 4.2.

Table 4.2: Constraints imposed on the battery base plate design

Constraint number	Constraint
C1,1	The plate must fit within the physical constraints of the jet ski hull without modification to the surrounding structure
C1,2	The base plate must be compatible with waterjet cutting capabilities

4.1.4 Relevant Codes and Standards

No Australian standard specifically governs the structural design of battery mounting plates for small electric watercraft. The design was therefore validated against the material yield strength of the selected aluminium alloy using FEA, with a minimum factor of safety of 2.0 applied to all load cases. The adopted factor of safety was established in consultation with project supervisors and is considered sufficient for the intended application.

4.1.5 Design Development

The base plate was developed from a pre-existing concept produced by a previous project member. Upon review, the design exhibited geometric interference with surrounding hull components and required structural assessment before further development. Modification was prioritised over a full redesign, as the existing dimensional envelope and mounting philosophy were largely compatible with the hull geometry, making resolution of interference conflicts and FEA validation the primary development tasks.

4.1.6 Structural Assessment of Existing Design

The existing base plate, as seen in Figure 4.1, featured a formed 5 mm aluminium construction with an integrated rear motor mounting section, four lifting points, a battery enclosure bolt pattern, and a forward aperture accommodating the front foil retraction mechanism. As this satisfied the majority of system requirements, it was adopted as the foundation for the final design.

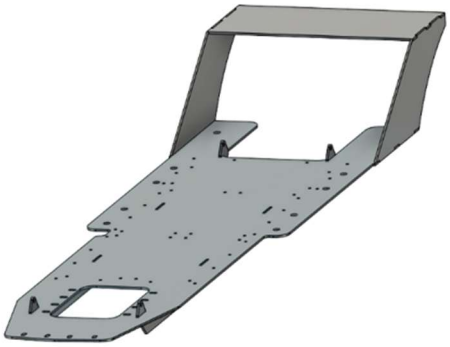

Figure 4.1: CAD model of the previous base plate

An FEA was conducted on the existing base plate to assess its structural adequacy under worst-case loading conditions, evaluating its capacity to support the battery assembly, front foil attachment, and rear foil thrust forces. This aimed to establish whether major structural modification was required, or whether geometric interference resolution alone would be sufficient.

The material properties were defined for Aluminium 5052-H34, as this was the material used in the previous construction. The properties are as follows (MatWeb, n.d.):

- Shear Modulus: 25.92GPa
- Youngs Modulus: 70.33GPa
- Poisson Ratio: 0.36
- Density: 2683 kg/m^3
- Yield Strength: 213.74MPa
- Ultimate Tensile Strength: 262MPa

The constraints applied to the analysis were applied at the hull bolt holes, assuming rigid bolts and no movement at the hull interface. Four load cases were considered to determine the structural capacity of the existing base plate; all derivations are provided in Appendix A4.

A free body diagram of the jet ski forces imposed by hydrodynamic forces are presented by Figure 4.2

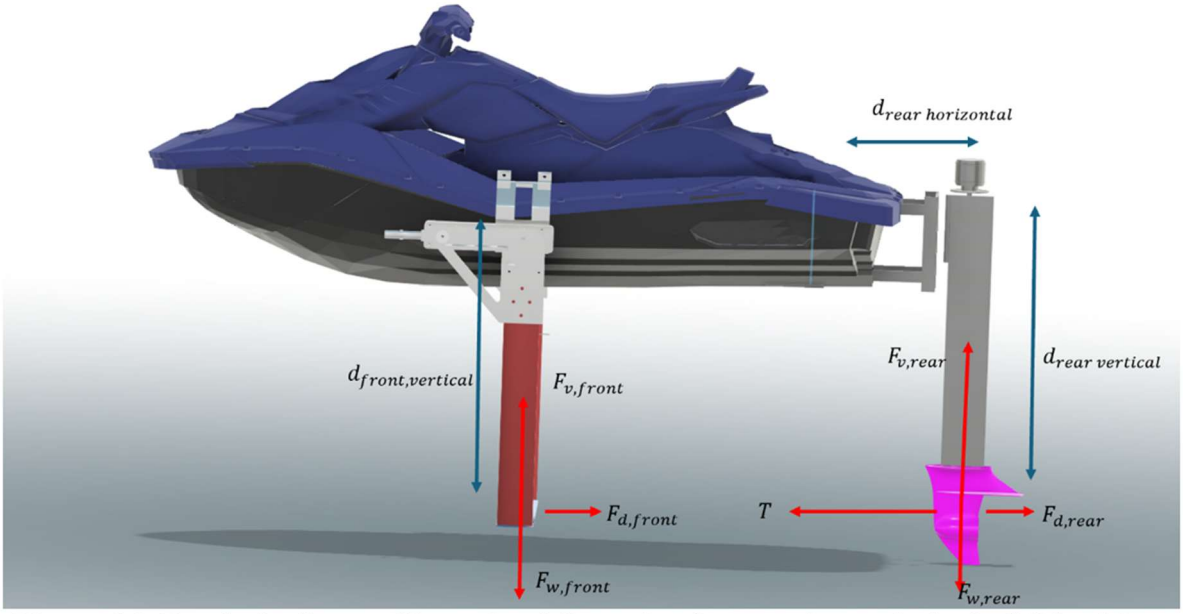

Figure 4.2: Free body diagram illustrating foil reaction forces acting on the hydrofoil jet ski.

The first load case considered the static weight of the battery assembly distributed across the battery mounting locations, establishing a baseline structural response. The weight was modelled as a uniform pressure load, as described by Equation 4.1.

$$\sigma_{Battery} = \frac{F_{Batteries}}{A_{Battery}} = \frac{m_{batteries}g}{A_{Battery}} \tag{4.1}$$

The resulting pressure load was determined to be 2516.5 Pa. The corresponding free body diagram is presented in Figure 4.3.

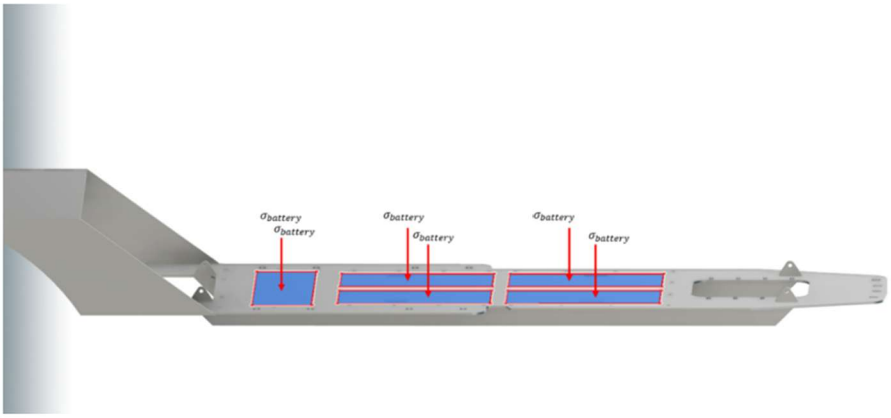

Figure 4.3: Battery load application locations used in the base plate FEA.

The second load case considered the rear foil reaction forces (lift, drag, thrust, and foil weight) transmitted through the base plate at the rear foil mounting interface, as seen in Figure 4.4. These combine to produce a resultant bending moment, transmitted to the base plate as vertical and horizontal forces at each bolt location. Through an iterative process, 25% of the total reaction force was determined to be the maximum load transmissible through the base plate whilst maintaining a factor of safety of 2.0, with the remaining 75% assumed to be transferred directly to the hull structure.

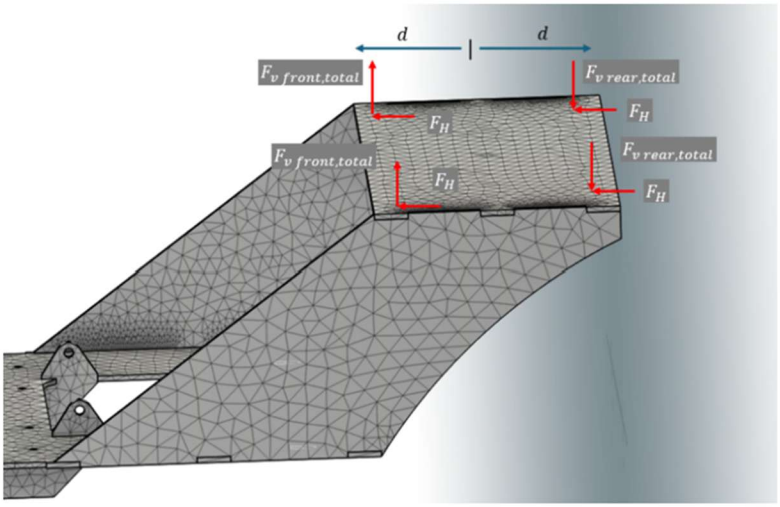

Figure 4.4: Rear hydrodynamic forces transmitted on rear plate.

The rear foil lift reaction is assumed to be transmitted through 50 × 50 mm washers at each M12 bolt location. Resultant forces are summarised in Table 4.3, with full derivations provided in Appendix A4.

Table 4.3: Final Resultant Forces applied on rear plate via hydrodynamic force on the rear foil

Final Resultant Forces/Moments	Derivation	Value	Applied Load (25% of Total)
Horizontal force	F_H	$877.0N$	$219.25N$
Total vertical force on front two bolts	$F_{v\ front,total}$	2061.5N	515.38N
Total vertical force on rear two bolts	$F_{v\ rear,total}$	-3345.5N	-836.38N

The front foil attachment reaction was distributed across the bolt holes surrounding the forward aperture, assuming the foil is positioned centrally relative to the bolt pattern. The resulting load distribution is illustrated in Figure 4.5.

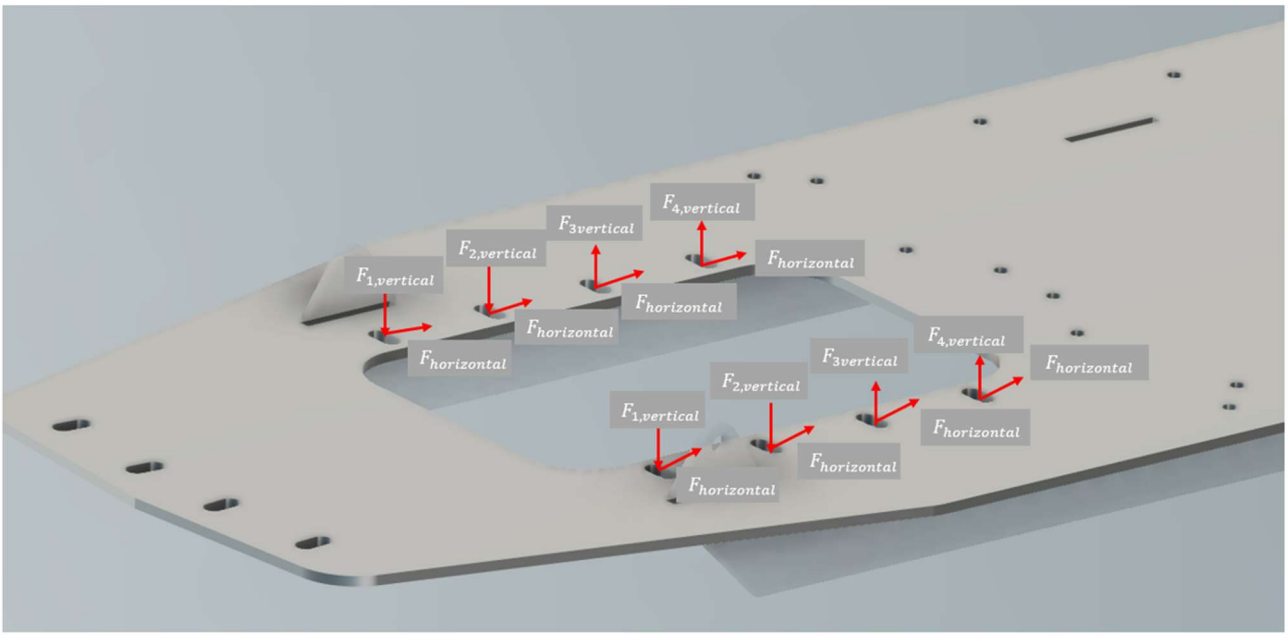

Figure 4.5: Front foil hydrodynamic forces transmitted on front of base plate.

Resultant forces at each bolt location are summarised in Table 4.4. The bending moment induced by foil drag force produce's upward reaction forces at the rear bolt locations and downward reaction forces at the front bolt locations.

Table 4.4: Final Resultant Forces applied on front of base plate from front foil hydrodynamic forces

Bolt Location	**Total Vertical Force per Bolt $F_{i,vertical}$**	**Total Horizontal Force per Bolt $F_{i,horizontal}$**
Rear far	1430N	52.08N
Rear close	683N	52.08N
Front close	-63N	52.08N
Front far	-810N	52.08N

Figure 4.6 illustrates the von Mises stress distribution from FEA of the base plate under combined loading from the battery weight, rear foil assembly attachment, and front foil assembly attachment

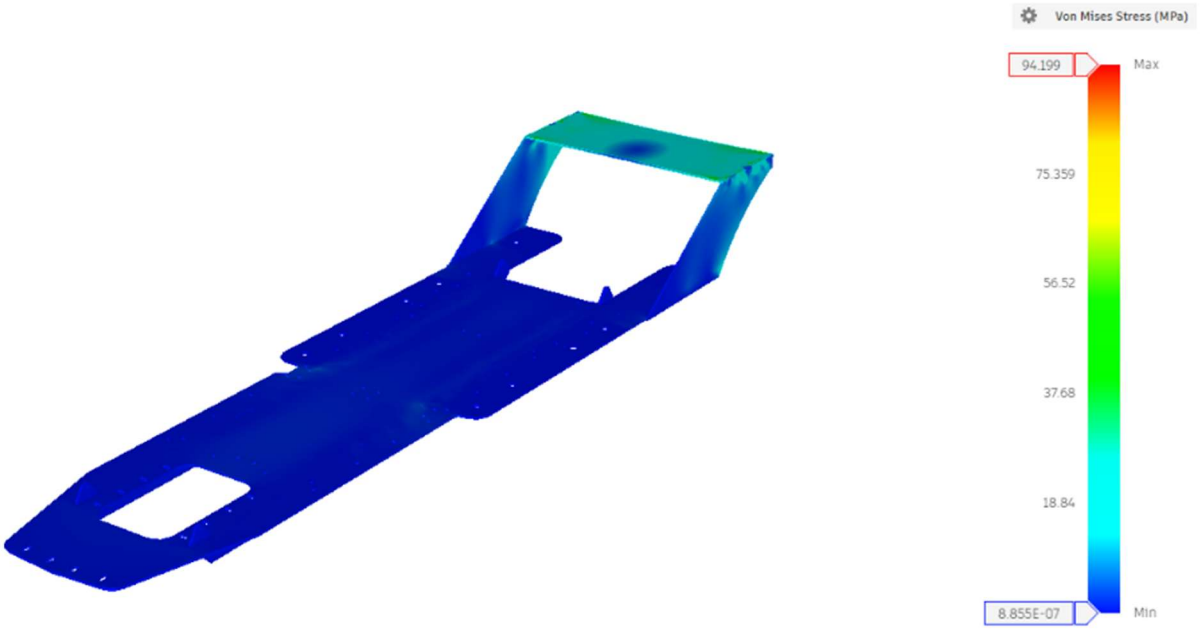

Figure 4.6: FEA von Mises stress distribution of the existing base plate under combined operational load cases.

The FEA results summarised in Table 4.5 indicate the existing base plate is structurally suitable for continued development, provided the majority of rear foil lift is transferred directly to the hull. On this basis, the existing design concept was retained and subsequent development focused on resolving geometric interference within the hull envelope.

Table 4.5: FEA results summary for the previous base plate under operating load cases.

Maximum Von Mises Stress (MPa)	Maximum Displacement (mm)	Minimum Factor of Safety	Safety Factor Target	Pass/Fail
94.20	3.286	2.30	2.0	Pass (2.30>2.0)

4.1.7 Interference Analysis and Design Resolution

Interference resolution followed an iterative physical-to-CAD methodology. The existing base plate was physically modified to resolve geometric conflicts within the hull envelope, with measurements taken from the modified plate used to update the CAD model, which then served as the fabrication reference. This approach allowed rapid fit verification without requiring full CAD iteration prior to physical validation. The modifications detailed in Appendix A3 resolved all geometric conflicts, producing the final base plate geometry.

4.2 Battery Waterproofing

4.2.1 Problem Definition

The high-voltage lithium battery pack must remain fully isolated from water ingress at all times. Moisture penetration presents a severe risk of short-circuit, fire, and explosion (National Fire Protection Association [NFPA], 2023), making waterproofing enclosure integrity the most critical design requirement of the project. No commercially available enclosure exists for the battery

configuration used, necessitating a bespoke design capable of achieving a marine-grade ingress protection rating while integrating structurally with the base plate and remaining compatible with the water-cooling system.

4.2.2 Design Requirements

The design requirements for the waterproofing enclosure are summarised in Table 4.6.

Table 4.6: Requirements for the battery waterproofing design

Requirement number	***Requirement***
R2,1	Prevent water ingress into the battery enclosure during operation, achieving a minimum IP65 rating.
R2,2	Enclosure panels must maintain internal structural stresses within a factor of safety of 2.0 under worst-case loading conditions.
R2,3	Design must be manufacturable using tools and processes available within the UWA engineering workshop.
R2,4	Ventilation must satisfy AS/NZS 3004.2-2014 clause 2.9.2.3.

4.2.3 Design Constraints

The design constraints imposed by the physical limitations of the existing jet ski platform are summarised in Table 4.7.

Table 4.7: Constraint imposed on the battery waterproofing design

Constraint number	***Constraint***
C2,1	Provide sufficient internal clearance above the battery pack to accommodate additional electrical components, with a minimum internal headspace of 60 mm.
C2,2	Dimensioned to fit within the physical constraints of the jet ski hull without modification to the surrounding structure.

4.2.4 Design Standards and Codes

AS/NZS 3004.2-2014 is relevant to the waterproofing enclosure design, requiring that lithium-ion battery ventilation airflow be in accordance with manufacturer specifications; where specific data is not provided, Clause 2.9.2.2 or 2.9.2.3 shall be applied (Standards Australia, 2014). Clause 2.9.2.3 governs natural ventilation and is expressed by Equation (4.2):

$$A = 100 q_v \tag{4.2}$$

Where:

- A is the minimum vent area (cm^2)
- q_v is the minimum ventilation rate (L/s)

As the manufacturer has not specified a minimum exhaust ventilation rate, this value must be calculated. Breather vents will be installed on the enclosure to satisfy this requirement.

No applicable standard was identified governing IP ratings for lithium battery enclosures in marine applications; however, literature indicates a minimum rating of IP65 is appropriate (Battery Council International, 2022), confirming the enclosure must be fully dust-tight and protected against water jets. Testing requirements for IP65 certification are specified in IEC 60529 (International Electrotechnical Commission [IEC], 2013).

4.2.5 Testing and Evaluation

Waterproofing verification was conducted with reference to the IP65 requirements of IEC 60529 (International Electrotechnical Commission [IEC], 2013). The standard requires the enclosure to be sprayed from all practicable directions under the following conditions:

- Delivery rate of 12.5 L/min
- Nozzle distance of 2.5 m to 3.0 m from the enclosure
- Minimum test duration of 3 minutes

A standard garden hose was used to approximate these conditions. While this does not precisely replicate the specified delivery rate, it provides a practical preliminary assessment of enclosure sealing integrity. FEA was also conducted to verify the enclosure would not yield under maximum internal pressure resulting from thermal expansion of gases generated by the battery pack during operation.

4.2.6 Design Development

An initial concept considered encasing the battery pack in heat shrink plastic wrap, which offered simplicity, low cost, and conformability (TE Connectivity, 2023). The design team rejected this approach for several reasons: longitudinal wrapping would enclose the entire base plate assembly, preventing additional components from being mounted and making installation impractical; sharp edges on the base plate and electrical components posed a significant puncture risk that would compromise waterproof integrity; and a heat shrink enclosure provides no means of accessing the battery pack once sealed, requiring full removal and reapplication for any maintenance. Figure 4.7 illustrates this concept.

Figure 4.7. Heat shrink plastic wrap enclosure concept for battery pack waterproofing (Marsen, n.d.).

4.3 Water-cooling System

4.3.1 Problem Definition

The outboard motor and ESC generate significant heat under sustained high-load operation due to resistive losses in the motor windings and switching losses in the power electronics. Without adequate thermal management, heat accumulation risks insulation degradation, motor derating, and thermal shutdown (Gieras, 2010). Active water cooling is therefore required to maintain both components within their rated operating temperatures.

4.3.2 Design Requirements

Motor cooling requirements were derived from the Maytech MTI120116 datasheet (Maytech, n.d.-a) and ESC cooling requirements from the Maytech MTSVESC7.5H datasheet (Maytech, n.d.-b). Shown by Table 4.8 and 4.9 respectively.

Table 4.8: Requirements for the water-cooling system design

Requirement number	***Requirement***
R3.1	The cooling system must maintain motor winding temperature below 120°C during sustained operation.
R3.2	A filtration device must be installed on the inlet line to prevent ingestion of debris that could damage the internal cooling circuit.
R3.3	The circuit must be fully sealed to prevent coolant or water ingress into the hull.
R3.4	Internal pipes must be flexible and compatible with the motor and ESC inlet and outlet barb connectors.
R3.5	The ESC must be maintained below 85°C, consistent with the default MOSFET thermal protection cutoff enforced by the VESC firmware [REF].
R3.6	All circuit components must be resistant to galvanic corrosion and seawater exposure.
R3.7	The circuit pump must provide sufficient pressure head to circulate coolant through the complete circuit.

Table 4.9: Constraints for the water-cooling system design

Constraint number	*Constraint*
C3.1	All components must be procured from commercially available suppliers within project budget constraints.
C3.2	Flexible tubing must have an outer diameter of less than 15 mm to fit within the hull envelope.
C3.3	Reducer fittings must be incorporated to accommodate the motor barb outer diameter of 10 mm and ESC cold plate barb outer diameter of 6 mm.

4.3.3 Design Standards and Codes

The cooling of rotating electrical machines is addressed by AS 1359.21 and IEC 60034-6 (Standards Australia, 1974; International Electrotechnical Commission [IEC], 1991), which classify cooling arrangements for electric motors but do not prescribe specific thermal limits for small marine applications. Design requirements were therefore derived from manufacturer specifications for the MTI120116 motor and MTSVESC7.5H ESC.

4.3.4 Health and Safety Considerations

The primary safety consideration is the proximity of the cooling circuit to high-voltage components including the battery pack and ESC. A coolant leak presents a risk of electrical short circuit, shock, or fire (Gieras, 2010). All hose connections must be verified leak-free prior to energising the electrical system. During operation, the sea strainer should be inspected regularly to prevent blockage-induced motor overheating.

4.3.5 Testing and Verification Method

The cooling circuit will be tested prior to energisation of the electrical system by running the pump with water and inspecting all connections, fittings, and hull penetrations for leakage. Any identified leaks will be rectified before commissioning.

4.3.6 Design Development

Initial concepts for the water-cooling system comprised a single open circuit, drawing seawater through an inlet scoop mounted on the foil strut, passing through the motor cooling jacket and ESC cold plate in series, before discharging overboard. The circuit would be sustained entirely by the motor's internal impeller pump, requiring no additional components beyond piping and fittings. This approach was attractive for its simplicity and low part count. The system architecture is illustrated by the P&ID presented in Figure 4.8.

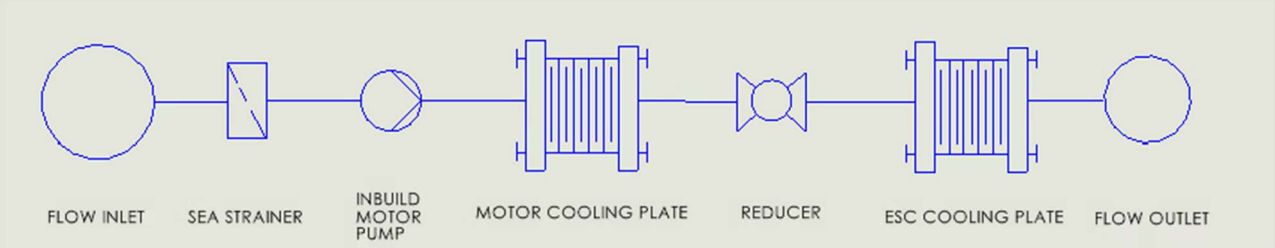

Figure 4.8: P&ID of the initial single open-circuit water-cooling concept.

Figure 4.9 illustrates the water-cooling system integration within the jet ski hull. Cold seawater is drawn in at the propeller and circulated upward through the motor, before being directed through the ESC and expelled back into the environment.

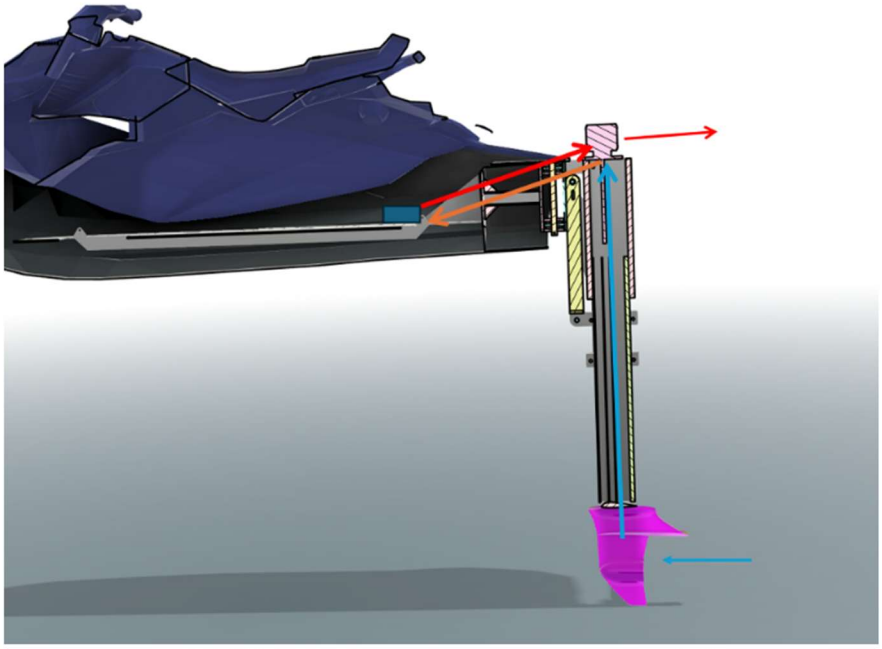

Figure 4.9: Water-cooling system flow path through the jet ski hull.

This design presented two significant issues. First, routing coolant through the motor cooling jacket before the ESC cold plate meant water arriving at the ESC had already absorbed heat from the motor, reducing the temperature differential available for ESC cooling. As the more thermally sensitive component, the ESC is particularly sensitive to receiving pre-warmed coolant. More critically, direct contact between raw seawater and the ESC cold plate introduced a corrosion risk. The cold plate integrated into the Maytech MTSVESC7.5H is constructed from aluminium, and prolonged seawater exposure would cause galvanic and salt-induced corrosion, degrading the cold plate over time (Davis, 1999). These issues necessitated a redesign separating the motor and ESC cooling into two independent circuits.

5. Results and Discussion

Results are presented for each of the three subsystems, the chassis base plate, battery waterproofing enclosure, and water-cooling system. Final designs and validation outcomes are discussed in the context of the requirements and constraints established in Section 4, with outstanding verification items identified where applicable.

5.1 Battery Base Plate Design and Discussion

5.1.1 Final Design Validation

The finalised base plate retains the core geometry and functional architecture of the existing design, incorporating targeted modifications to resolve the geometric interferences identified during the design review. Principal features remain consistent with the preceding iteration, including the integrated rear motor mounting section, four-point lifting arrangement, and bolt hole patterns for battery mounting, enclosure attachment, and hull interface. A clearance aperture at the forward end accommodates the front foil retraction mechanism. The final design and its features are presented in Figure 5.1, with key parameters summarised in Table 5.1.

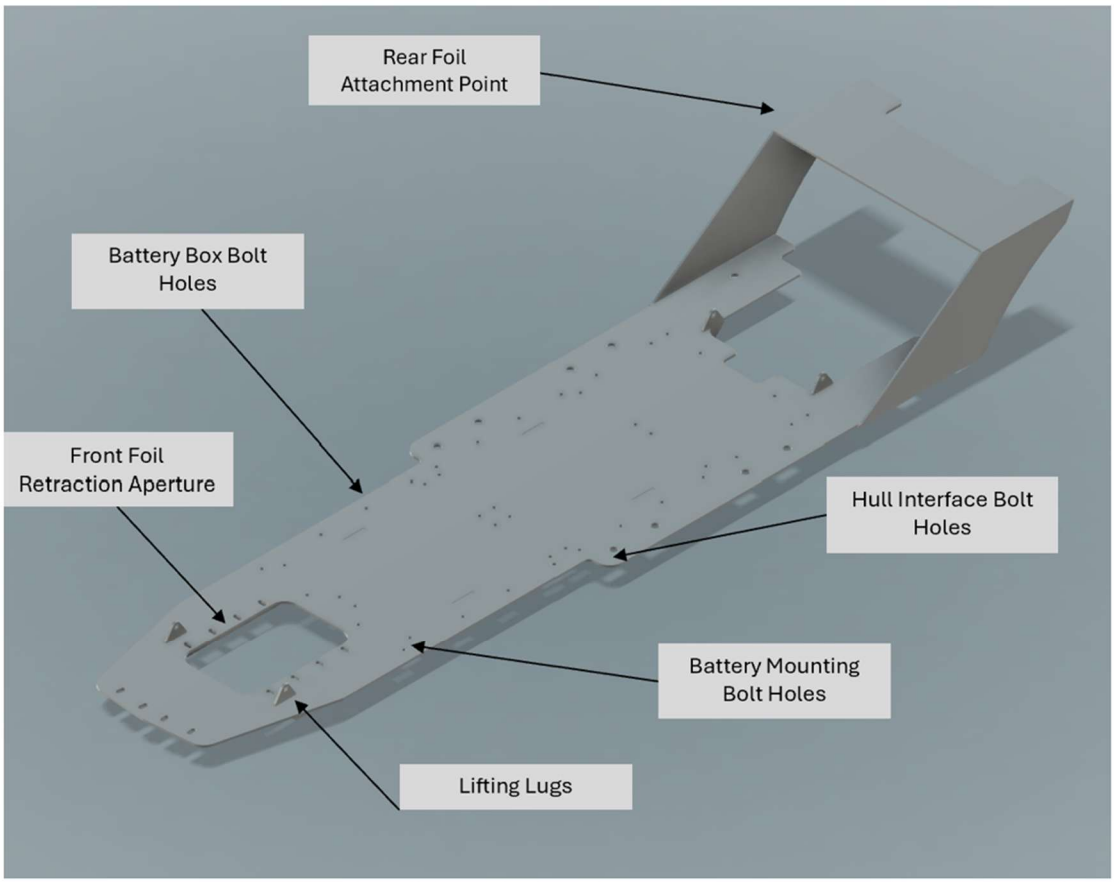

Figure 5.1: Annotated CAD model of the redesigned AL5052 battery base plate, showing key interface features and mounting provisions.

Table 5.1: Battery base plate key design parameters.

Key Parameters	***Value***
Hull interface bolt diameter	M16
Battery mounting bolt hole diameter	M7
Battery enclosure bolt hole diameter	M7
Plate Thickness	5mm
Forward aperture dimensions	260mm by 170mm
Largest plate width	500mm
Plate length	1780mm
Material	AL5052
Rear foil attachment plate dimensions	220mm x 510mm
Rear foil attachment plate height	220mm

The base plate incorporates interlocking stepped joints along the mating edges as demonstrated by figure 5.2, allowing adjacent plates to locate into one another during assembly. This ensures accurate alignment during welding and eliminates the need for external fixturing.

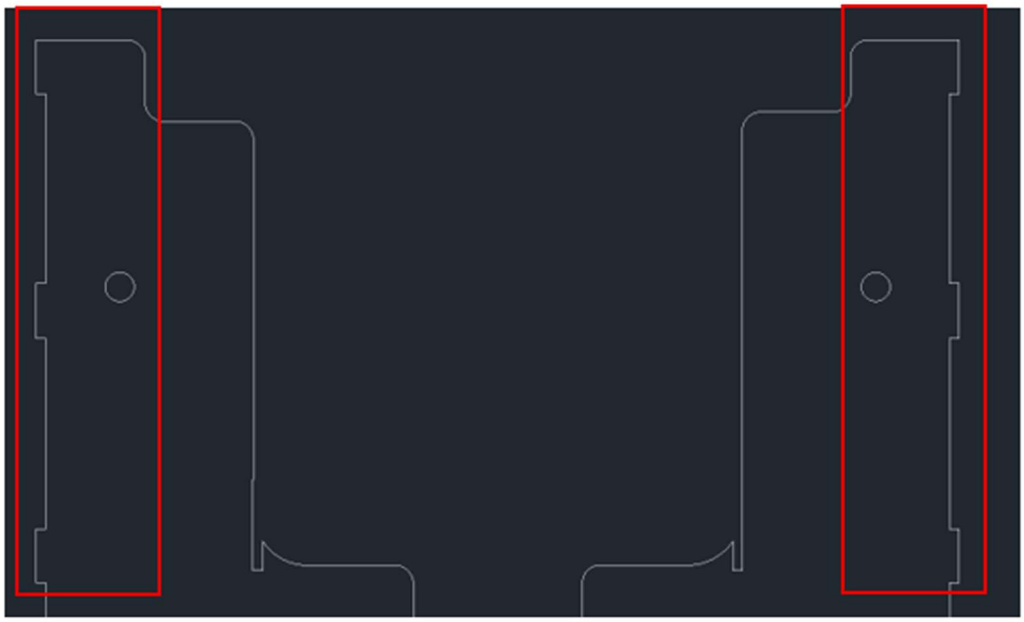

Figure 5.2: Base plate interlocking stepped joint detail, with mating edge regions highlighted in red.

5.1.2 Material Validation

Al 5052-H34 was selected based on the material comparison in Table 5.2. Stainless steel grades were rejected due to their high density and poor strength-to-weight ratio, and carbon fibre composite rejected for its prohibitive cost and susceptibility to seawater-induced fatigue degradation. Al 5052-H34 offers the best combination of strength-to-weight ratio, corrosion resistance, weldability, and cost for this application.

Table 5.2: Material comparison for base plate selection across key structural and environmental properties. Data Adopted from (Callister and Rethwisch 2020).

	Strength to weight Ratio (σ_y/ρ)	**Corrosion resistance (mm/year)**	**Cost (AUD/kg)**	**Density**
Units	$(MPa \cdot m^3/kg)$	$(mm/year)$	(AUD/kg)	(kg/m^3)
AL5052-H34	~ 0.072	0.01~0.05	$\sim \$6-10$	~ 2680
304 Stainless Steel	~ 0.045	0.1~0.5	$\sim \$1.5-3$	~ 7850
316 Stainless Steel	~ 0.026	0.002~0.02	$\sim \$8-15$	~ 8000
Carbon Fibre Composite	~ 0.6	Non-corrosive	$\sim \$60-150$	~ 1600

5.1.3 Structural Validation – Operating loads

The finalised base plate was evaluated under the same four load cases applied to the preceding design iteration: static battery weight, 100% of the front foil hydrodynamic load, and 25% of the rear foil hydrodynamic load, representing the governing condition for structural adequacy. The resulting von Mises stress distribution and displacement field are presented in Figure 5.3.

The analysis yielded a peak von Mises stress of 98.07 MPa and a maximum displacement of 3.396 mm, corresponding to a factor of safety of 2.18 against the yield strength of Al 5052. This exceeds the minimum required factor of safety of 2.0, confirming the plate will not undergo permanent deformation under the anticipated operating loads. The peak stress concentration occurs at the motor mounting interface, consistent with the expected load path under combined loading.

The 25% rear foil load share was determined iteratively by progressively increasing the rear foil load contribution until the factor of safety approached the 2.0 threshold, establishing the maximum load the base plate can sustain while maintaining structural adequacy. Figure 5.3 presents the stress distribution under full rear foil load transmission, yielding a peak von Mises stress of 391.71 MPa, which exceeds the material yield strength. It is therefore recommended that the rear foil mounting be designed to transfer the majority of hydrodynamic load directly into the hull structure rather than through the base plate.

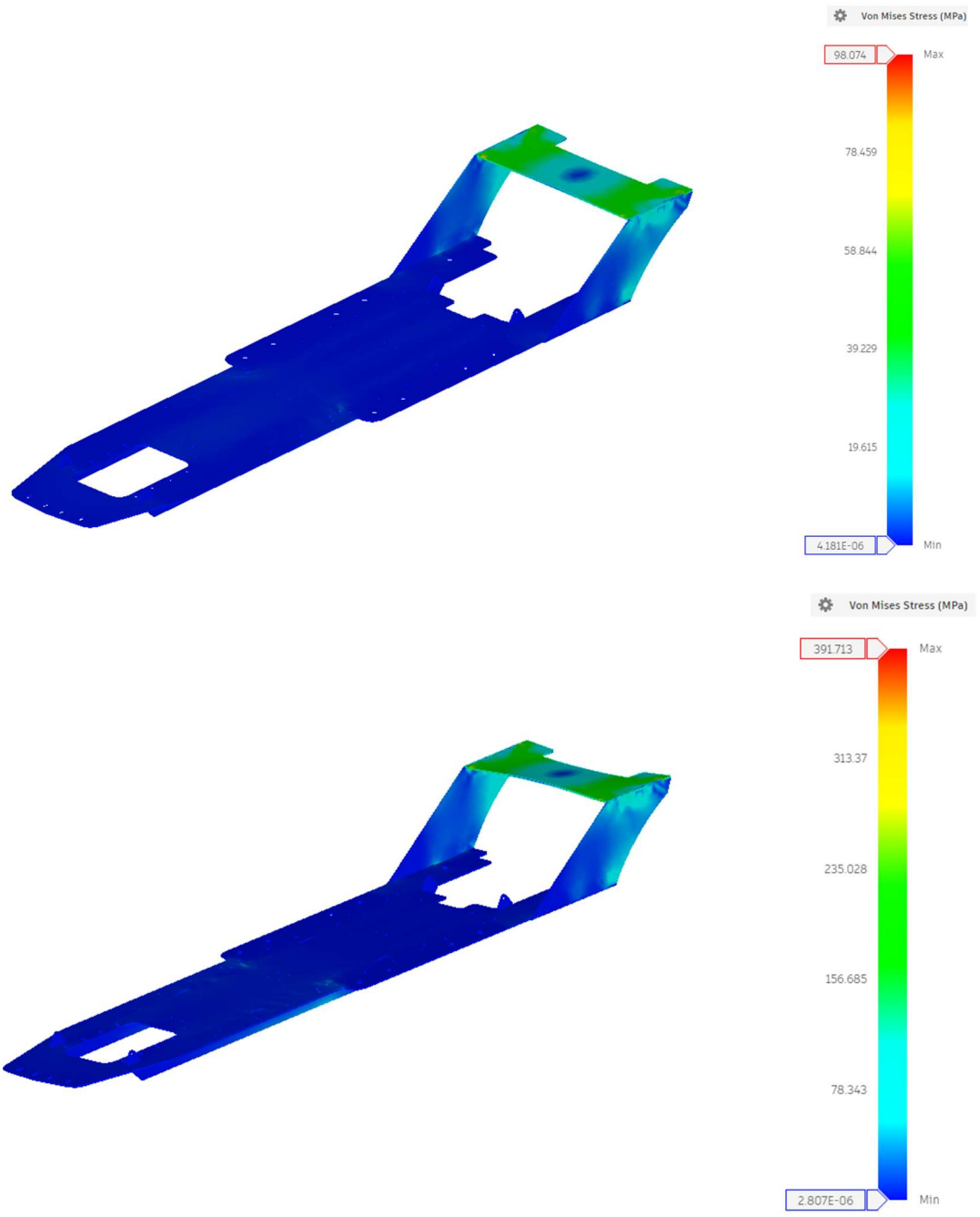

Figure 5.3: von Mises stress distribution of the base plate under Case 1 (25% rear foil load, peak 98.07 MPa, top) and Case 2 (100% rear foil load, peak 391.71 MPa, bottom).

Table 5.3 summarises the FEA results for both load cases, where Case 1 represents the operational condition with 25% rear foil hydrodynamic load and Case 2 represents the non-operational upper bound at 100%.

Table 5.3: FEA structural results for base plate loading cases under 25% and 100% rear foil hydrodynamic load.

Case	Maximum Von Mises Stress (MPa)	Maximum Displacement (mm)	Minimum Factor of Safety	Factor of Safety target	Pass/Fail
Case 1	98.07	3.396	2.18	2.0	Pass (2.18 > 2.0)
Case 2	391.71	11.36	0.546	2.0	Fail (0.546 < 2.0)

The FEA loading cases were derived from the hydrodynamic lift and drag forces, calculated using Equations (5.1) and (5.2) (Çengel & Cimbala, 2018):

$$L = \frac{1}{2}\rho V^2 C_L A \tag{5.1}$$

$$D = \frac{1}{2}\rho V^2 C_D A \tag{5.2}$$

These equations assume steady uniform inflow, which does not capture the turbulent and unsteady conditions experienced near the free surface at operating speed. A CFD simulation would be required to obtain a more accurate representation of the hydrodynamic forces.

5.1.4 Base Plate Final Design Requirement Compliance

The finalised base plate was evaluated against the requirements and constraints established in Section 4.1.2, with outcomes summarised in Tables 5.4 and 5.5. All requirements were satisfied, with a minimum factor of safety of 2.18 achieved across the governing load cases, confirming the base plate is structurally adequate for the intended application. All design constraints were also satisfied, with zero hull interference upon installation, bolt hole alignment achieved without hull modification, and the selected material and thickness compatible with waterjet cutting.

Table 5.4. Battery base plate design requirements and compliance verification.

Requirement number	**Outcome**
R1.1	Factor of safety of 2.18 under governing load cases — **Satisfied**
R1.2	Base plate bolt holes align with all eight pre-existing hull locations — **Satisfied**
R1.3	20 × M4 mounting bolt holes incorporated for enclosure attachment — **Satisfied**
R1.4	AL5052 provide excellent corrosion resistance in marine environment— **Satisfied**
R1.5	All weld joints confirmed accessible from at least one side — **Satisfied**
R1.6	Base plate provides a dedicated rear foil mounting platform and forward attachment points for the front foil — **Satisfied**

Table 5.5: Battery base plate design constraints and compliance outcomes

Measurable number	**Outcome**
C1,1	Zero interference confirmed upon physical installation of the base plate — **Satisfied**
C1,2	Al 5052 at 5 mm thickness confirmed compatible with waterjet cutting — **Satisfied**

5.2 Waterproofing Case Design and Discussion

5.2.1 Final Design Overview

The battery enclosure protects the lithium battery modules and associated electrical components from water ingress during marine operation. The final design is illustrated in Figure 5.4, with key design parameters summarised in Table 5.6.

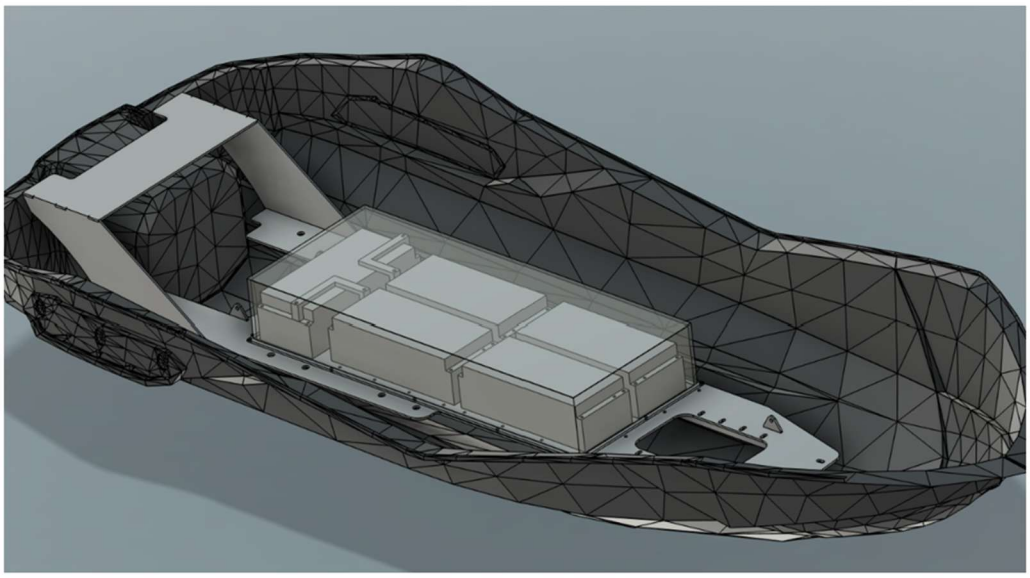

Figure 5.4: Fusion 360 CAD model of the acrylic battery enclosure installed within the jet ski hull.

Table 5.6: Acrylic battery enclosure key design parameters.

Key Parameters	**Value**
Material	Acrylic (PMMA)
Gasket material	EPDM
Breather vent model	JDA12PA/SW × 2
Pressure relief valve model	VENT-MS4NME-O8002
Internal dimensions	960 mm x 395 mm x 168 mm
Bolt holes size	5 mm
Number of bolts	20
Panel thickness	6 mm

The primary sealing interface consists of a closed-cell EPDM gasket seated between the enclosure lip flange and the battery base plate, supplemented by solvent cement bonding the acrylic panels. Three pressure management devices are incorporated: two breather valves managing pressure differentials up to 7 kPa, and one spring-loaded relief valve opening at 12 kPa to protect against lithium battery off-gassing. Pre-existing base plate penetrations were sealed with silicone, and rubber washers installed beneath the battery mounting bolts prevent water ingress from below. The two external busbars required refabrication to fit within the enclosure geometry.

5.2.2 Design Manufacture - Acrylic Battery Enclosure

Engineering drawings were produced from the Fusion 360 model and panel DXF files submitted to the university workshop for laser cutting, with assembly drawings provided in Appendix B1. Panels were joined using solvent cement applied by workshop technicians, chemically fusing the acrylic surfaces into a continuous sealed bond (Trinseo, 2022). Bolt holes were drilled post-fabrication to ensure alignment with the base plate, and breather vents were installed after waterproofing verification to avoid compromising the test. The manufactured enclosure is shown in Figures 5.5

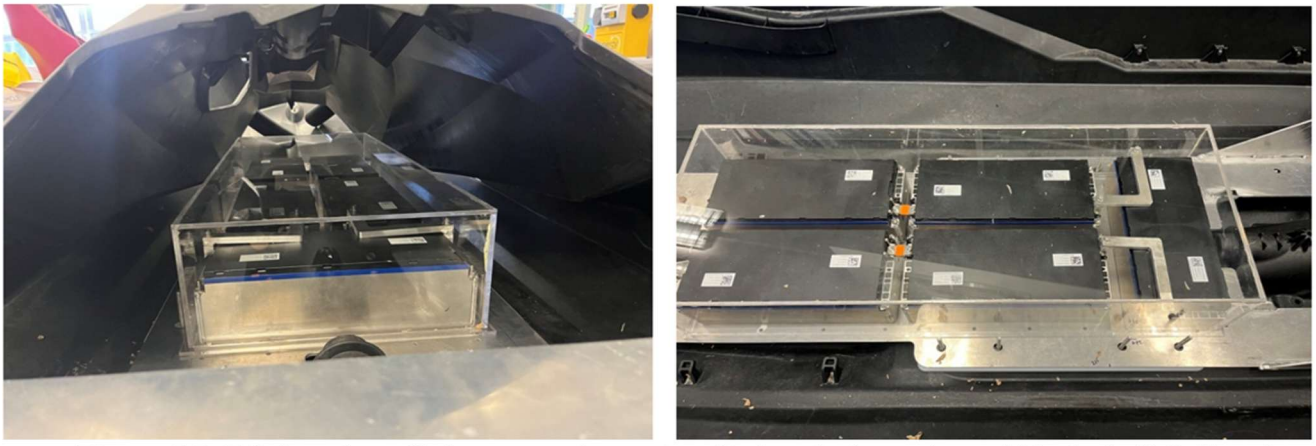

Figure 5.5: Fabricated acrylic battery enclosure installed on the base plate within the hull (left) and top view showing battery modules housed within the enclosure (right).

5.2.3 Design Manufacture - Battery Busbar Manufacture

The two external busbars required refabrication to accommodate the revised battery arrangement, reorienting from a horizontal outward configuration to vertical mounting over the top of the batteries, as shown in Figure 5.6 with engineering drawings provided in Appendix B1.

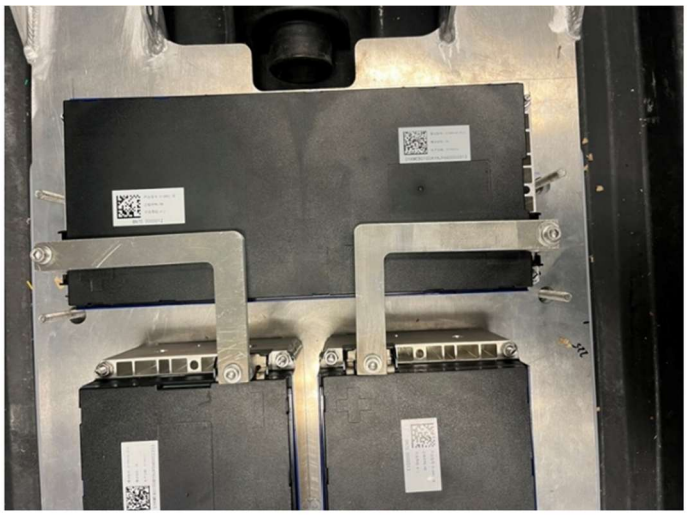

Figure 5.6. Refabricated external busbars reoriented to mount vertically over the battery pack.

5.2.4 Verification and Testing Result— IP65 Hose Test

Waterproofing verification was conducted by applying water across all external surfaces and joints using a garden hose, with the flow rate adjusted to approximately 13 L/min in accordance with IEC 60529 IP65 test conditions (International Electrotechnical Commission [IEC], 2013). Post-test inspection revealed moisture on the internal walls, indicating the enclosure had failed the test. Figure 5.7 identifies the ingress locations; the solvent cement bond along the lip flange was found to be inconsistent, with visible gaps in adhesive coverage.

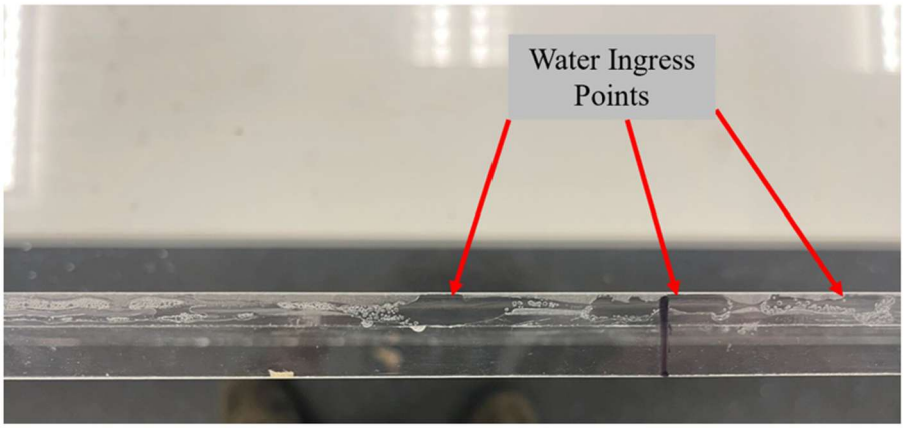

Figure 5.7. Water ingress points observed along the base plate joint during leak testing.

The enclosure was refurbished by applying a silicone sealant bead along all internal panel joints as a secondary seal, shown in Figure 5.8. The hose test was repeated and inspection of the internal walls revealed no moisture, confirming the leakage paths had been eliminated. The enclosure is considered watertight and suitable for electrical integration.

Figure 5.8. UWA engineering workshop applying silicone to internal panel joints

5.2.5 Pressure Relief Analysis

The battery enclosure requires pressure management to prevent air expansion from loading the enclosure walls and joints during operation. Two mechanisms were selected: membrane breather vents for continuous passive pressure equalisation, and a spring-loaded pressure relief valve for overpressure protection. Full specifications are provided in Appendix B3.

Battery thermal behaviour was modelled using a four-node lumped capacitance system, with discrete nodes representing the battery pack, internal air, acrylic walls, and aluminium plate (Incropera et al., 2007). The energy balance equation for each node is as follows:

Battery pack:

$$m_b c_b \frac{dT_b}{dt} = \dot{Q}_b - h_{ba} A_b (T_b - T_a) \tag{5.3}$$

Internal air:

$$m_a c_a \frac{dT_a}{dt} = h_{ba} A_b (T_b - T_a) - h_{aw} A_w (T_a - T_w) - h_{aw} A_{al} (T_a - T_{w.al}) \tag{5.4}$$

Acrylic walls:

$$m_{ac} c_{ac} \frac{dT_{w,ac}}{dt} = h_{aw} A_{ac} (T_a - T_{w,ac}) - h_{wo,ac} A_{ac} (T_{w,ac} - T_\infty) \tag{5.5}$$

Aluminium plate:

$$m_{al} c_{al} \frac{dT_{w,al}}{dt} = h_{aw} A_{al} (T_a - T_{w,al}) - h_{wo} A_{al} (T_{w,al} - T_\infty) \tag{5.6}$$

Appendix B3 defines the model parameters and their derived values. The ODEs govern heat transfer between nodes through convection and are integrated numerically using the fourth-order

Runge-Kutta method over a 2-hour simulation window (Chapra & Canale, 2015). The volumetric flow rate resulting from air thermal expansion is modelled by Equation (5.7).

$$\dot{V}(t) = \left(\frac{V_{air}}{T_a + 273.15}\right) \cdot \frac{h_{ba}A_b(T_b(t) - T_a(t)) - h_{aw}A_w(T_a(t) - T_w(t)) - h_{aw}A_{al}(T_a(t) - T_{w.al}(t))}{m_a c_a} \quad (5.7)$$

Figure 5.9 displays the resultant temperatures of each node with respect to time as well as the flow rate with respect to time.

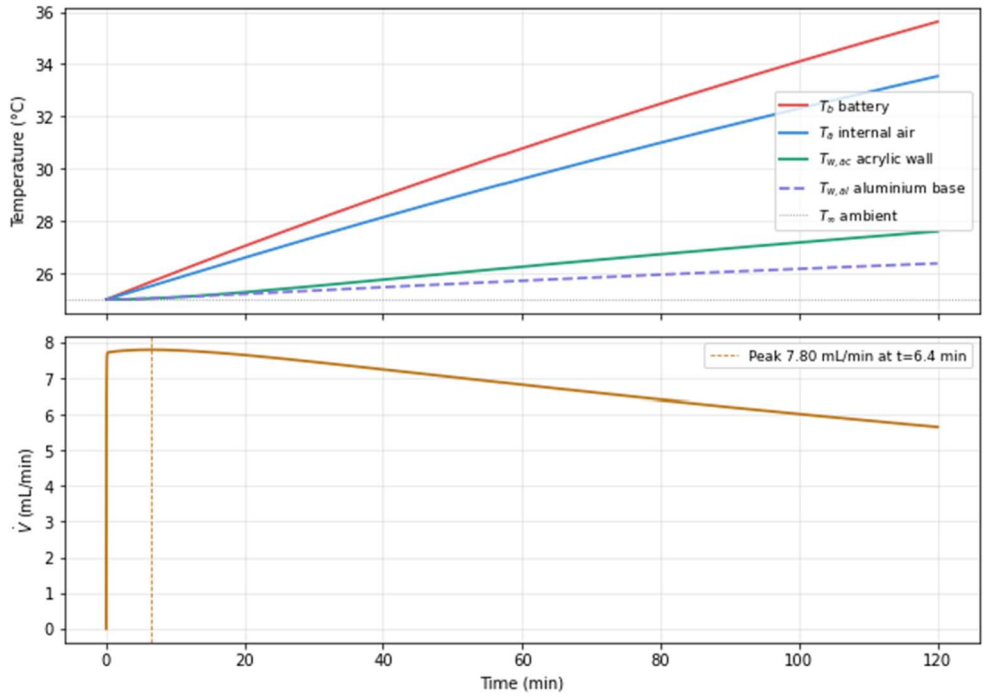

Figure 5.9: Four-node lumped capacitance thermal model outputs — node temperatures over time (top) and volumetric flow rate over time (bottom).

The maximum volumetric flow rate, occurring at t = 6.4 min as shown in Figure 5.9, reaches 7.80 mL/min. The two membrane breather vents provide a combined flow capacity of 172.7 mL/min, far exceeding the calculated peak demand.

The primary modelling assumptions are that each node is spatially uniform in temperature with internal gradients neglected, convection coefficients are constant throughout operation, and the enclosure is thermally sealed except through the defined conductance paths, conduction through bolt fixings and cable gland penetrations is neglected, making the model conservative (Incropera et al., 2007). Internal air-to-wall and external convection coefficients are literature-adopted values for still air, which is conservative as any airflow during operation would increase heat dissipation and reduce steady-state temperatures (Çengel & Ghajar, 2015). The external coefficient incorporates a

linearised radiation coefficient to account for radiative exchange between the outer surfaces and surroundings (Howell et al., 2016); this linearisation is valid given the modest wall-to-ambient temperature difference. Internal convection coefficients were left unchanged as enclosed air is effectively transparent to thermal radiation and internal surface radiation is negligible at the temperatures encountered.

5.2.6 Acrylic Enclosure Structural Verification

The breather vents operate at a pressure differential of 7 kPa. FEA of the acrylic enclosure confirmed the design remains within elastic limits at this pressure, as shown in Figure 5.10.

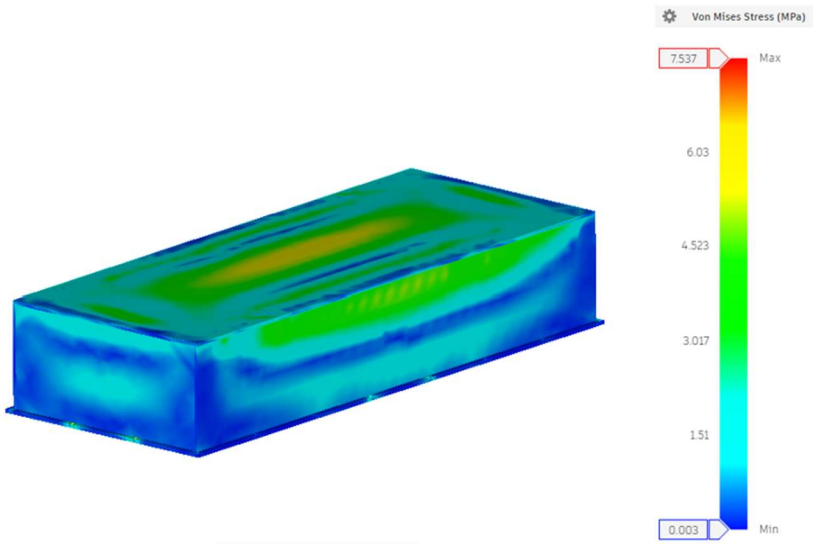

Figure 5.10: von Mises stress distribution of the acrylic battery enclosure under 7 kPa internal pressure, maximum stress 7.537 MPa.

The FEA results indicate a maximum von Mises stress of 7.537 MPa under the maximum operating pressure, corresponding to a factor of safety of 5.307 against yielding. The pressure relief valve opens at 12 kPa, ensuring internal pressure cannot exceed this threshold. Figure 5.11 confirms the enclosure remains within the fatigue limit under the resulting cyclic stress with a factor of safety of 2.07.

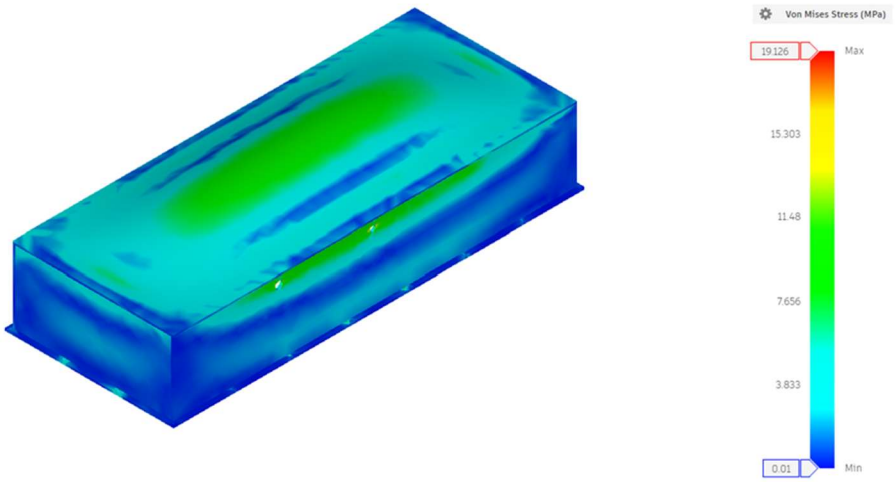

Figure 5.11: von Mises stress distribution of the acrylic battery enclosure under 12 kPa internal pressure, maximum stress 19.126 MPa.

The FEA model assumed fully bonded contact between all panel interfaces. In practice, the solvent cement joint was not uniform across the full bonded lip, as evidenced by Figure 5.7, which shows discontinuities in the bond line. These unbonded regions represent localised stress concentrations not captured by the simulation, meaning the true factor of safety at these locations may be lower than the FEA result suggests.

5.2.7 Ventilation Requirement Verification

The ventilation requirement was verified against AS/NZS 3004.2-2014 (Standards Australia, 2014), which specifies that the minimum vent area must satisfy Equation (4.2):

$$A > 100q_v$$

Where:

- A is the effective vent area cm^2
- q_v is the minimum exhaust ventilation rate (L/s)

Using two JDAE12PA/SW membrane breather vents with 10 mm internal diameters and an ePTFE membrane porosity of 85% (Amphenol LTW, 2023), the effective open area is 1.34 cm². The calculated peak ventilation demand of $10.27\ mL/min$ corresponds to $1.71 \times 10^{-4}\ L/s$, giving a required minimum vent area of $0.017\ cm^2$. The effective vent area of $1.34\ cm^2$ satisfies this requirement with substantial margin, confirming compliance with AS/NZS 3004.2-2014.

5.2.8 Design Requirement and Constraint Compliance

The final enclosure design was assessed against the design requirements and constraints established in Section 4.2, with compliance summarised in Tables 5.7 and 5.8.

Table 5.7: Battery enclosure design requirements and compliance verification.

Requirement/Constraint	Compatibility
R2.1	IP65 hose test revealed no leakage, dripping, seepage, cracking, or joint separation after full test duration. - **Satisfied**
R2.2	Pressure relief analysis yielded a factor of safety of 5.307 against material yield strength, exceeding the minimum required factor of safety of 2.0. - **Satisfied**
R2.3	Enclosure panels fabricated entirely using the university workshop laser cutter with no external manufacturing required. - **Satisfied**
R2.4	Effective vent area of 1.34 cm² exceeds the minimum required area of 0.017 cm², satisfying AS/NZS 3004.2-2014 clause 2.9.2.3 - **Satisfied**

Table 5.8: Battery enclosure design constraints and compliance verification

Constraint Number	Compatibility
C2,1	Internal headspace above the battery pack measures 63mm, satisfying the minimum 60mm requirement - **Satisfied**
C2,2	Enclosure height of 168 mm fits within the jet ski hull without structural modification; busbars were refabricated to eliminate geometric interference - **Satisfied**

5.3 Water-cooling Design and Discussion

5.3.1 Final Design Overview

The final water-cooling design comprises two independent circuits: a raw seawater loop for the motor and a closed freshwater loop for the ESC. The motor circuit draws seawater through an inlet scoop mounted on the rear foil strut, which remains submerged below the waterline during operation. Coolant is driven by the motor's internal impeller pump through the motor cooling jacket before being discharged overboard through the transom. Coolant supply lines are routed through the foil mast, with a sea strainer installed on the inlet line to prevent debris ingestion that could damage the impeller or obstruct the circuit. The MTI120116 motor is purpose-built for raw water cooling via an internal impeller; compliance with the 120°C winding temperature limit is assumed by manufacturer design intent (Maytech, n.d.-a). The P&ID for this circuit is presented in Figure 5.12.

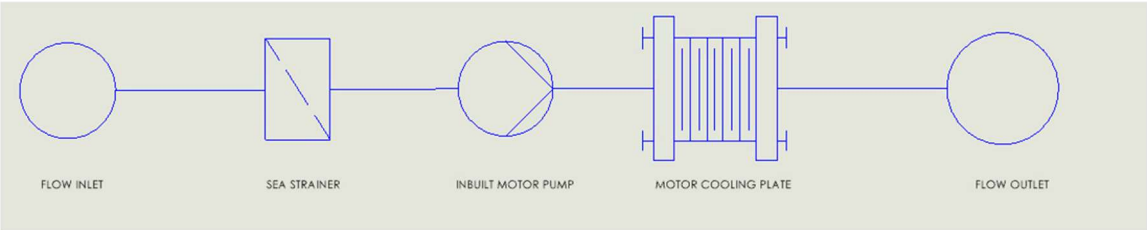

Figure 5.12: P&ID of the motor raw water-cooling circuit.

The ESC cooling circuit is a closed freshwater loop, isolated from seawater to protect the integrated aluminium cold plate of the Maytech MTSVESC7.5H from galvanic and salt-induced corrosion (Davis, 1999). Housed within the battery enclosure, the ESC is cooled by a dedicated 12V DC brushless pump circulating coolant through the cold plate, a brass water-to-air radiator, and a freshwater reservoir before returning to the pump. The P&ID for this circuit is presented in Figure 5.13.

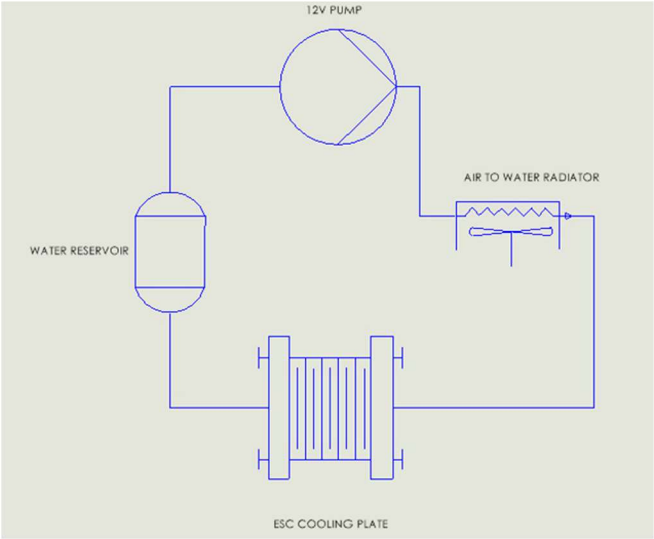

Figure 5.13: P&ID for the ESC cooling system

5.3.2 Component Selection and Procurement

All components for the ESC closed-loop circuit were procured from commercial suppliers to minimise cost. A double-layer brass radiator with G1/4 ports was selected for material compatibility with the ESC cold plate barbs, maintaining a consistent wetted material throughout the circuit to minimise galvanic corrosion risk (Davis, 1999). Brass G1/4 barb connectors were selected on the same basis. A 12V DC brushless pump, powered via a DC-DC step-down converter from the 72V battery pack, circulates coolant through the loop. A 270 mL reservoir provides a buffer volume and air bleed point during filling. PVC flexible hose was used for all internal connections due to its flexibility, chemical resistance, and low cost (IPEX, 2022). Distilled water mixed with an anticorrosion additive was selected as the working fluid for additional corrosion protection (Prestone, 2023).

5.3.3 ESC Heat Exchanger Area Verification

The selected radiator face area was verified against the thermal requirements of the ESC using the closed-loop liquid cooling model derived by Simons (2002). The governing equation expresses ESC surface temperature as a function of heat load, cold plate thermal resistance, heat exchanger effectiveness, and the heat capacity rates of both the water and air streams.

$$T_{ESC} = q_L \left(R_{cp} + \left(\frac{1}{\varepsilon C_{min}} - \frac{1}{C_w} \right) \right) + T_a \tag{5.8}$$

With radiator face area as the independent variable, the air-side heat capacity rate is:

$$C_a = \dot{m} c_a = \varphi \rho A v_{\perp} c_a = 3134.63A \text{ W/K}$$

where C_{min} is taken as the smaller of C_a and C_w. Two distinct operating regimes exist depending on radiator area: when $A \leq 0.0512$ m^2, the air side is the limiting resistance; when A exceeds 0.0512 m^2, the water side becomes the limiting resistance, $C_{min} = C_w = 160.37$W/K, and area no longer appears in the expression.

The radiator is positioned on the top of the hull; therefore, airflow does not act normal to the radiator face. The air velocity through the radiator was conservatively taken as the component of inflow velocity perpendicular to the radiator face:

$$v_{\perp} = v_{inflow} sin\theta \tag{5.9}$$

The angle was roughly 45°, Figure 5.14 shows this visually, and the inflow velocity taken as:

$$v_{\perp} = 0.707 v_{inflow} \tag{5.10}$$

Figure 5.14: Fusion 360 render illustrating the radiator mounting position on the hull deck and inflow air velocity direction relative to the radiator face.

T_{ESC} converges to a constant value of 59°C, representing the minimum temperature achievable through radiator area increase alone at the design operating speed of 10 knots.

$$T_{ESC} = \begin{cases} 54.76 + \dfrac{0.2170}{A}, & \mathrm{A} \leq 0.0511\mathrm{m}^2 \\ 59℃, & A > 0.0511\mathrm{m}^2 \end{cases} \tag{5.11}$$

Figure 5.15 illustrates T_{ESC} across both regimes. The selected radiator (188.4 cm², 157 mm × 120 mm) operates in the air-limited regime, yielding a predicted ESC temperature of 77.8°C. Although the MTSVESC7.5H does not publish an explicit junction temperature limit, the VESC firmware enforces a default MOSFET thermal cutoff at 85°C (Vedder, 2023), giving a design margin of 7.2°C.

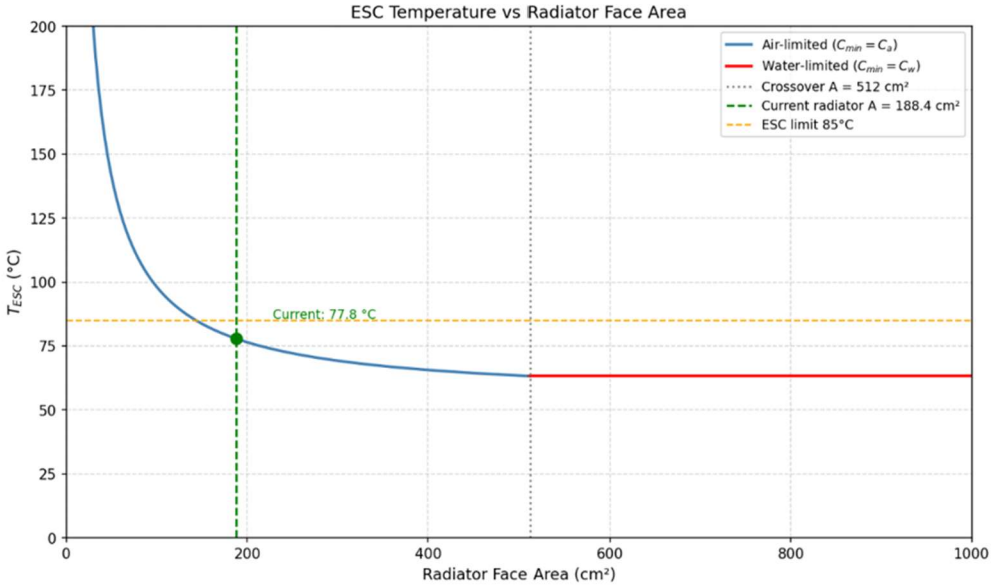

Figure 5.15: ESC temperature vs radiator face area

An ESC efficiency of 98% was adopted from published literature (Kim et al., 2019), yielding a heat load of q_L= 680 W. The cold plate thermal resistance was taken as R_{cp}= 0.05°C/W, representing the lower bound of the range published by Advanced Thermal Solutions (2017) (Advanced Thermal Solutions, 2017). Heat exchanger effectiveness was assumed as ε = 0.5, representative of a single-pass crossflow configuration under ram airflow (Incropera et al., 2007), this assumption carries the greatest model uncertainty, as no manufacturer data was available to verify it, a reduction to ε = 0.4 would noticeably raise the predicted ESC temperature. Full parameter details are provided in Appendix C2.

The operating flow rate was estimated using the Darcy-Weisbach equation applied to a 2 m PVC hose run of 5 mm internal diameter, with the pump curve approximated as linear between rated maximum head and flow. An iterative solution yielded an operating point of 2.33 L/min (0.0389 kg/s). This analysis accounts for pipe friction only, minor losses from fittings, bends, and internal passages were excluded, meaning the true flow rate is likely somewhat lower and will be refined once system geometry is finalised.

The predicted ESC temperature of 77.8°C carries inherent uncertainty due to the assumed heat exchanger effectiveness and cold plate thermal resistance. Notably, the MTSVESC7.5H is rated for 300A continuous operation without water cooling, rising to 400A with cooling (Maytech, n.d.-b); as the jet ski is unlikely to approach these currents in operation, ESC cooling is precautionary rather than a critical thermal requirement.

5.3.4 Waterproof Verification

The closed-loop ESC circuit was verified by running the pump and inspecting all connections, fittings, and hull penetrations for leakage, with none identified. Leak testing of the motor raw water circuit could not be completed as the motor has not yet been wired to the battery pack, and remains as future work prior to commissioning.

5.3.5 System Assembly

The radiator is proposed for mounting on the forward hull deck to maximise ram airflow exposure during operation. Hose runs would be routed internally through the hull to the ESC enclosure, with all penetrations sealed to maintain watertight integrity. Full installation remains as future work due to time constraints. The proposed system layout is shown in Figure 5.16, with water-cooling components positioned for reference in Figure 5.17.

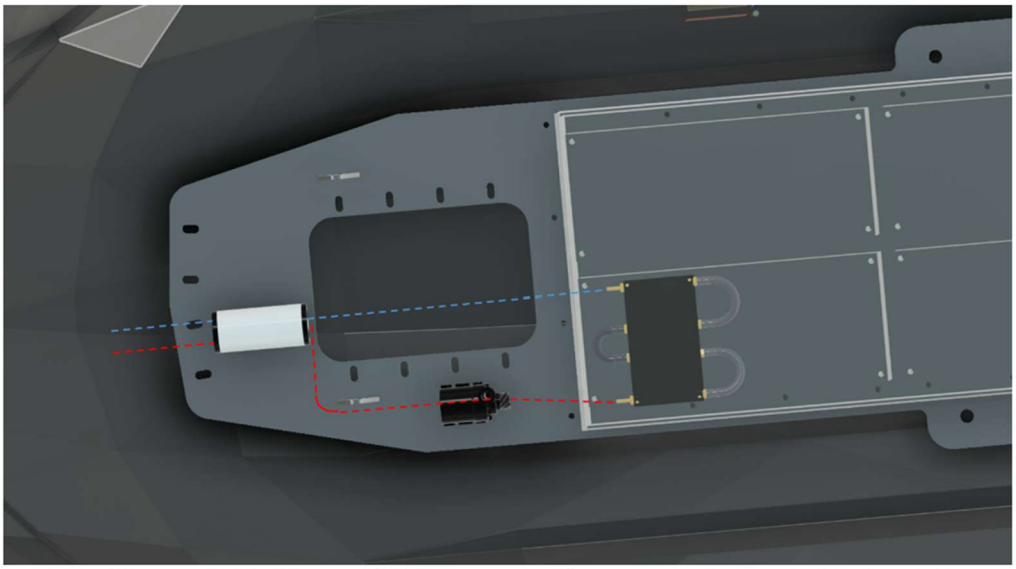

Figure 5.16: Planned ESC water-cooling system layout in Fusion 360.

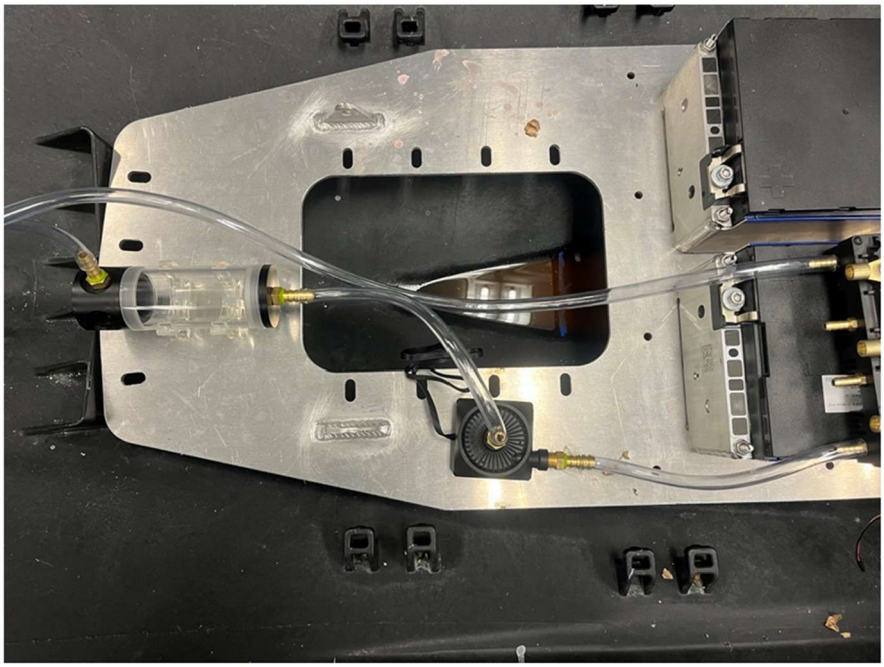

Figure 5.17: Water-cooling components positioned on the base plate for reference.

5.3.6 Design Requirements Compliance

Tables 5.9 and 5.10 summarise the water-cooling system design requirement and constraint compliance respectively.

Table 5.9: Water-cooling system design requirement compliance.

Requirement/Constraint	Compatibility
Motor Cooling Requirements	
R3.1	Motor circuit uses manufacturer-designed raw water cooling via internal impeller; compliance with 120°C winding limit assumed by design intent **- Assumed Satisfied**
R3.2	Sea strainer installed on motor circuit inlet line to prevent debris ingestion - **Satisfied**
R3.3	ESC circuit leak tested with pump running, no leakage identified at any connection, fitting, or hull penetration. Motor circuit leak test pending commissioning. – **Partially Satisfied**
R3.4	PVC flexible hose used throughout; reducer fittings incorporated to match motor (10 mm) and ESC (6 mm) barb diameters. -**Satisfied**
R3.5	Predicted ESC temperature of 77.8°C at design operating conditions, satisfying the 85°C MOSFET thermal cutoff with a margin of 7.2°C - **Satisfied**
R3.6	Consistent brass wetted surfaces in ESC circuit; distilled water with anticorrosion additive selected to minimise galvanic and corrosion risk. - **Satisfied**
R3.7	Iterative Darcy-Weisbach analysis yielded an operating flow rate of 2.33 L/min against a system head of approximately 2.5 m, within the pump's rated capacity of 3.5 m.**- Satisfied**

Table 5.10: Water-cooling system design constraint compliance.

Design Constraints	
C3,1	All components procured from commercial suppliers within budget constraints. - **Satisfied**
C3,2	PVC tubing with 11 mm outer diameter selected, satisfying the maximum 15 mm outer diameter constraint. - **Satisfied**
C3,3	Reducer fittings not required, the adoption of two independent circuits eliminates the diameter mismatch between motor and ESC barb connectors. – **Satisifed**

6. Conclusions & Future Work

This project addressed three mechanical engineering subsystems of UWA's electric hydrofoil jet ski: the battery base plate, battery waterproofing enclosure, and water-cooling system for the outboard motor and ESC.

The base plate redesign resolved geometric interference identified in the existing concept while retaining its dimensional envelope and mounting philosophy. Structural validation confirmed a factor of safety of 2.18 under the governing load case, satisfying the minimum requirement of 2.0. The base plate cannot sustain full rear foil hydrodynamic loading, a factor of safety of 0.546 was obtained under 100% rear foil load, and it is recommended that the rear foil mounting be designed to transfer the majority of load directly into the hull structure. CFD analysis is recommended to improve hydrodynamic load estimates beyond the steady uniform inflow assumption adopted here. The battery enclosure achieved IP65 waterproofing following remediation with a secondary silicone sealant bead after initial hose testing identified bond line discontinuities in the solvent cement joint. Pressure relief analysis confirmed breather vent capacity substantially exceeds peak ventilation demand, and FEA validated structural adequacy under operating pressure with a factor of safety of 5.307. It is recommended that future builds treat secondary silicone sealing as a standard fabrication step and that a consistent solvent cement application procedure be established. Future design iterations should target IP68 certification given that capsizing represents a realistic worst-case operational scenario, under which the enclosure would be subjected to sustained hydrostatic pressure rather than surface splash loading. Given the catastrophic consequences of water ingress into a high-voltage battery system, sealing adequacy under full submersion should be verified in future work.

The water-cooling system adopted a dual-circuit architecture, a raw seawater loop for the motor and a closed freshwater loop for the ESC, driven by the corrosion risk of seawater exposure to the aluminium ESC cold plate. The closed-loop ESC circuit was verified leak-free, and thermal modelling predicts an ESC operating temperature of 77.8°C, satisfying the 85°C firmware protection limit with a 7.2°C margin. Motor circuit leak testing and ESC radiator installation remain as immediate future work prior to commissioning, and motor operating temperature should be measured under full cooling system operation once the drivetrain is commissioned, as hardware constraints prevented thermal validation during this project.

The three subsystems addressed advance the prototype toward operational water trials, a necessary step in Oceanomatics' evaluation of the technology for commercial recreational use. Future students should prioritise commissioning of the motor circuit, full ESC loop installation, and integration testing under operational conditions.

7. References

CSIRO. (2026). *Low emissions technologies for maritime decarbonisation*. Commonwealth Scientific and Industrial Research Organisation. https://www.csiro.au/en/research/technology-space/energy/Decarbonising-Industry-Transport/ASLET

Erbe, C. (2013). *Underwater noise of small personal watercraft (jet skis)*. *The Journal of the Acoustical Society of America, 133*(4), EL326–EL330. https://pubmed.ncbi.nlm.nih.gov/23556699/

Ricardo. (2025). *What role will electrification play in the maritime market?* https://www.ricardo.com/en/news-and-insights/industry-insights/what-role-will-electrification-play-in-the-maritime-sector

Candela. (2023). *Candela C-8 electric hydrofoil boat*. https://candela.com/candela-c-8/

Suh, J. C., Lee, D. H., & Rhee, S. H. (2021). *Hydrodynamic performance analysis of a hydrofoil-supported high-speed craft*. *Journal of Marine Science and Engineering, 9*(6), 611. https://doi.org/10.3390/jmse9060611

Submersible Motor Engineering. (2016). *UWA electric jetski project*. https://www.smeng.com.au/uwa-electric-jetski-project/

Federation of American Scientists. (n.d.). *PHM Pegasus class hydrofoil missile patrol craft*. https://man.fas.org/dod-101/sys/ship/phm.htm

International Hydrofoil Society. (n.d.). *Early hydrofoils*. https://foils.org/library/bibliograpy/early-hydrofoils/

Loibner, D. (2018, March 23). *Hydrofoils: Past and renaissance*. Professional BoatBuilder. https://www.proboat.com/2018/03/hydrofoils-past-and-renaissance/

America's Cup. (2024). *AC75 yacht class*. https://www.americascup.com/en/ac75

Fliteboard. (2024). *Electric hydrofoil surfboards*. https://fliteboard.com/

Fraunhofer ICT. (2021). *Waterproof battery systems for marine and offshore electrification*. Fraunhofer Institute for Chemical Technology. https://www.ict.fraunhofer.de/

International Electrotechnical Commission. (2013). *IEC 60529: Degrees of protection provided by enclosures (IP code)*. IEC.

Liu, K., Yamamoto, K., & Morikawa, K. (2022). *A review of technologies and materials for sealing lithium-ion battery packs in electric vehicles*. *Journal of Energy Storage, 52*, 104824. https://doi.org/10.1016/j.est.2022.104824

Techspray. (2023). *Conformal coating and encapsulation guide for electronics protection*. https://www.techspray.com/

Acrylic Sheet Form. (2023). *Acrylic vs polycarbonate in marine applications*. https://www.acrylicsheetform.com/

Curbell Plastics. (2024). *Acrylic vs. polycarbonate comparison guide*. https://www.curbellplastics.com/

International Electrotechnical Commission. (2002). *IEC 62262: Degrees of protection provided by enclosures for electrical equipment against external mechanical impacts (IK code)*. IEC.

Trinseo. (2022). *Bonding and fabrication characteristics of acrylic and polycarbonate materials*. https://www.trinseo.com/

Campbell, F. C. (2010). *Structural composite materials*. ASM International.

Siriruk, A., Penumadu, D., & Raju, K. S. (2020). *Effects of seawater immersion on the fatigue behaviour of carbon fibre reinforced vinyl ester composites*. *Composite Structures, 236*, 111857. https://doi.org/10.1016/j.compstruct.2019.111857

Callister, W. D., & Rethwisch, D. G. (2020). *Materials science and engineering: An introduction* (10th ed.). Wiley.

Davis, J. R. (1993). *Aluminum and aluminum alloys*. ASM International.

Necemer, B., Klemenc, J., & Nagode, M. (2021). *Influence of rolling direction on fatigue behaviour of aluminium alloy sheets under cyclic loading*. *International Journal of Fatigue, 146*, 106140. https://doi.org/10.1016/j.ijfatigue.2021.106140

The Aluminum Association. (2022). *Properties and applications of 5xxx series aluminium alloys*. https://www.aluminum.org/

Gieras, J. F. (2010). *Permanent magnet motor technology: Design and applications* (3rd ed.). CRC Press.

Gundabattini, E., Kuppan, R., Solomon, D. G., & Babu, T. S. (2021). *A review on thermal management techniques for electric vehicle motors*. *Renewable and Sustainable Energy Reviews, 152*, 111674. https://doi.org/10.1016/j.rser.2021.111674

Pyrhönen, J., Jokinen, T., & Hrabovcová, V. (2014). *Design of rotating electrical machines* (2nd ed.). Wiley.

International Energy Agency. (2023). *Reducing emissions from shipping*. https://www.iea.org/energy-system/transport/shipping

Shenzhen Tritek Limited. (n.d.). *3P4S/2P6S NMC battery module*. https://www.lifepo4-battery.com/Products/CALB-Battery/3P4S-2P6S-NMC-Battery-Module.html

MatWeb. (n.d.). *AA 5052-H34 aluminium alloy material properties*. https://www.matweb.com/

National Fire Protection Association. (2023). *NFPA 855: Standard for the installation of stationary energy storage systems*. NFPA. https://www.nfpa.org/

Standards Australia. (2014). *AS/NZS 3004.2:2014 Electrical installations—Marinas and recreational boats—Part 2: Recreational boats installations*. Standards Australia.

Battery Council International. (2022). *Battery enclosure protection requirements and IP ratings for lithium battery systems*. https://batterycouncil.org/

TE Connectivity. (2023). *Heat shrink tubing and wraparound products for electrical insulation and environmental sealing*. https://www.te.com/

Marsen. (n.d.). *Heat shrink wrap PVC*. https://marsen.com.au/product/heat-shrink-wrap-pvc/

International Electrotechnical Commission. (1991). *IEC 60034-6: Rotating electrical machines – Part 6: Methods of cooling (IC code)*. IEC.

Standards Australia. (1974). *AS 1359.21-1974 Rotating electrical machines – Methods of cooling*. Standards Australia.

Çengel, Y. A., & Cimbala, J. M. (2018). *Fluid mechanics: Fundamentals and applications* (4th ed.). McGraw-Hill Education.

Incropera, F. P., DeWitt, D. P., Bergman, T. L., & Lavine, A. S. (2007). *Fundamentals of heat and mass transfer* (6th ed.). John Wiley & Sons.

Chapra, S. C., & Canale, R. P. (2015). *Numerical methods for engineers* (7th ed.). McGraw-Hill Education

Howell, J. R., Siegel, R., & Mengüç, M. P. (2016). *Thermal radiation heat transfer* (6th ed.). CRC Press.

Amphenol LTW. (2023). *JDAE12PA/SW waterproof pressure equalization vent specifications*. https://www.amphenolltw.com/

Vedder, B. (2023). *VESC firmware documentation and thermal protection settings*. https://vesc-project.com/

Simons, R. E. (2002). *Estimating parallel plate-fin heat sink thermal resistance*. ElectronicsCooling, 8(1). https://www.electronics-cooling.com/

Incropera, F. P., DeWitt, D. P., Bergman, T. L., & Lavine, A. S. (2007). *Fundamentals of heat and mass transfer* (6th ed.). John Wiley & Sons.

8. Appendix

Appendix A1: Base plate drawings

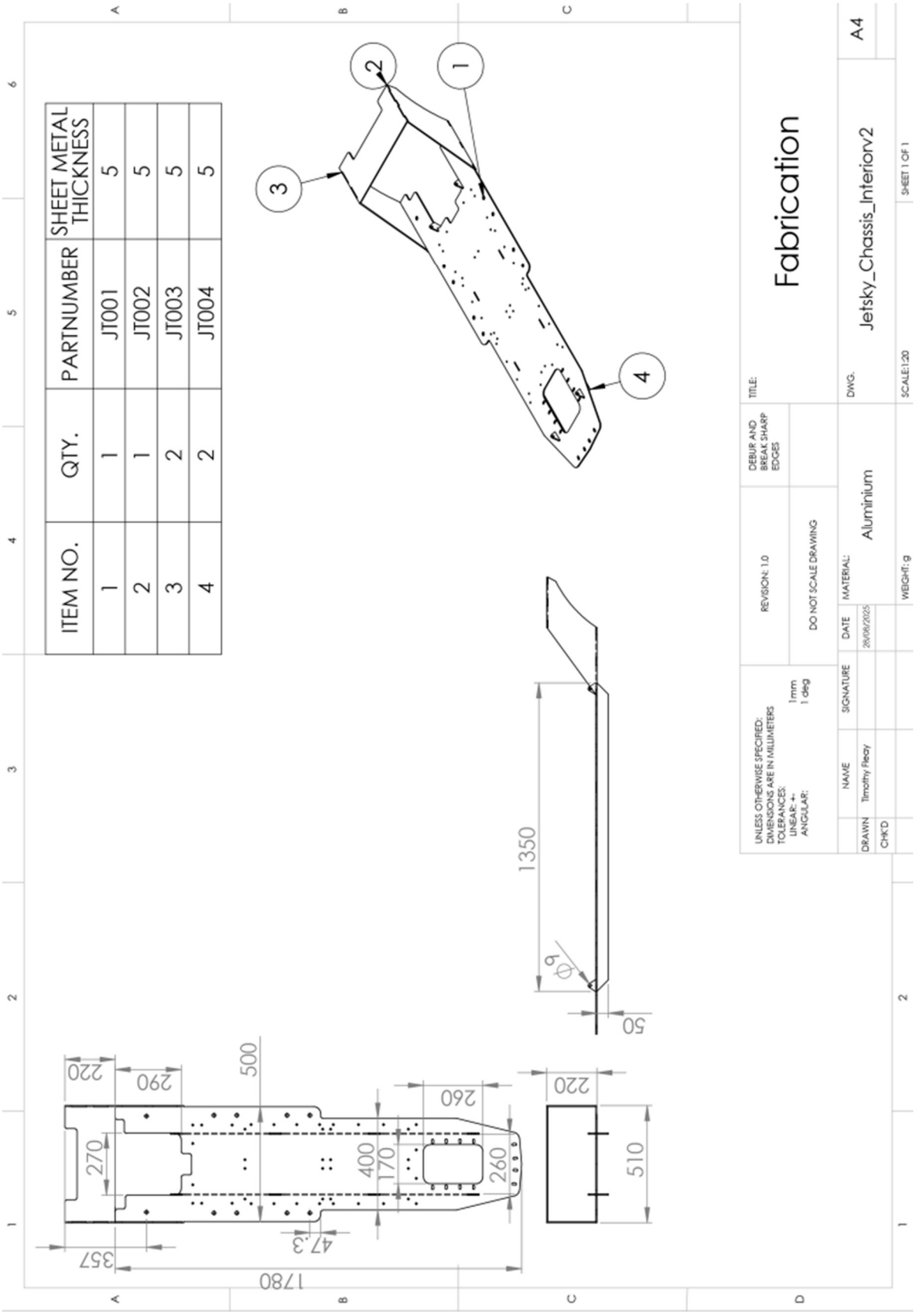

Figure A1.1: Base plate chassis drawings

Appendix A2: Base plate cost table and part tables

Table A2.1: Base plate cost table

Cost Item	Cost per Unit	Quantity	Subtotal ($AUD)
Raw Stock Material Cost			
AL5052	$120	1	$120
M6 x 120mm Bolts	$2.2	20	$44
M6 washers	$0.2	40	$8
M6 nuts	$0.4	20	$8
Total Raw Material Cost			**$180**
Fabrication and Assembly Costs			
Slake Cutting			$413.50
Sealed Fabrication Welding			$180
Total Manufacturing Costs			**$593.5**
Total Cost			**$773.50**

Table A2.2: Battery bolt part table

Component: Metric HT 8.8 Bolts Zinc Plated		*WA Bolts*
Size	M6 x 120mm	
Quantity	20	
Strength Grad	8.8	
Material	Zinc plated carbon steel	
Tensile Strength	800MPa	
Yield Strength	640MPa	

Table A2.3: Battery nut part table

Component: ***Standard M6 Hex Nuts***	*WA Bolts*
Size	M6
Material	Zinc plated carbon steel
Quantity	20

Table A2.4: Battery washer part table

Component: ***Standard M6 flat washer***	*WA Bolts*
Size	M6
Material	Zinc plated carbon steel
Type	Flat round washer
Standard	Metric ISO
Quantity	40

Appendix A3: Base plate interference changes

Table A3.1: Base plate interference changes

Physical Changes Made	***Changes Made***	***Changes Implemented on SolidWorks***
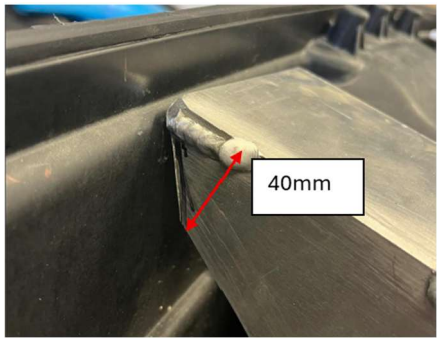	*The top corner of the rear base plate flange was found to interfere with the rear hull structure. A 40mm chamfer was introduced at the corner to provide the necessary clearance*	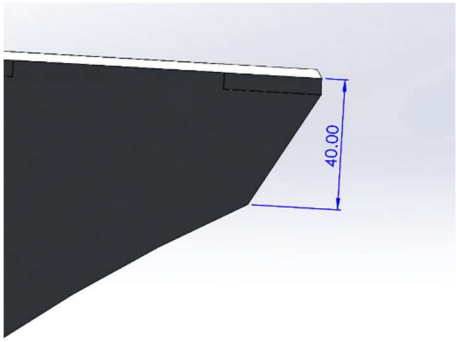
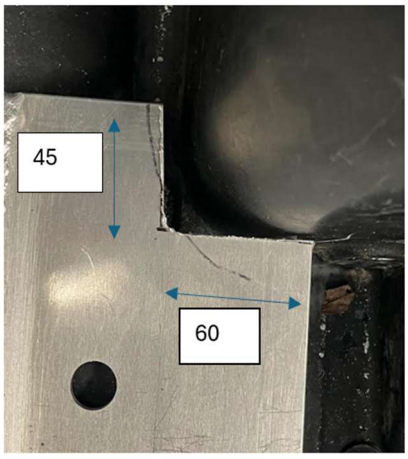	*The curved inner corner of the rear hull interfered with the adjacent edge of the base plate. A 60mm × 40mm rectangular cutout was introduced at the corresponding location on the base plate to provide clearance around the hull corner geometry.*	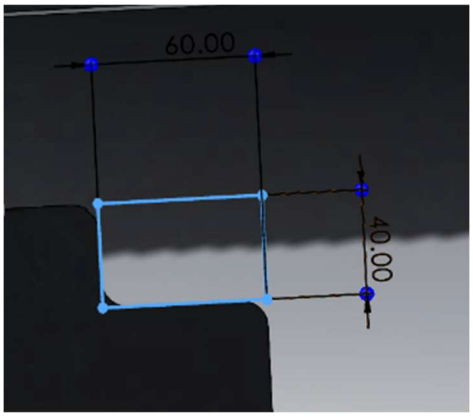
	*Cylindrical plugs on the hull structure were found to protrude into the base plate envelope, preventing flush seating of the plate. The plugs were removed and the base plate edge profile was modified to sit flush against the hull surface*	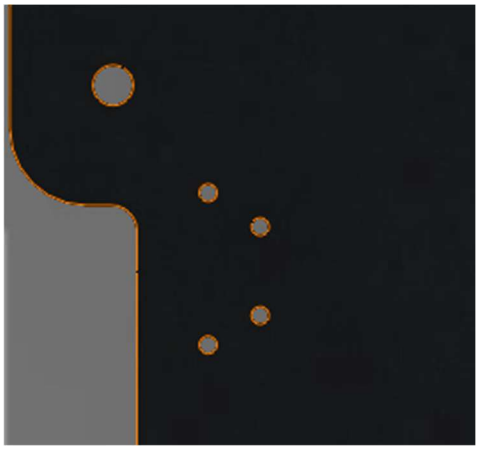

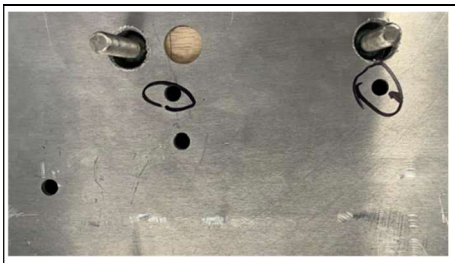	*Redundant bolt holes from the previous design iteration were removed*	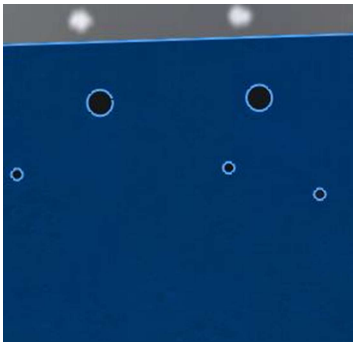
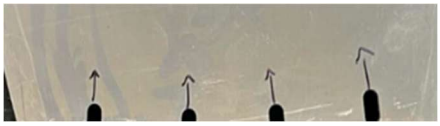	*The forward edge of the base plate interfered with the front hull structure. The front mounting bolt holes were repositioned rearward to allow the plate to seat correctly within the hull envelope.*	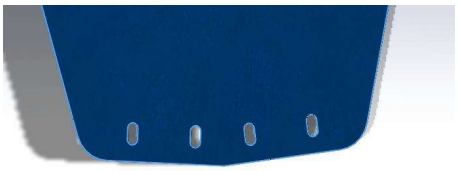
	*The battery enclosure mounting bolt holes were misaligned with the enclosure footprint and were shifted 15mm to restore correct alignment.*	
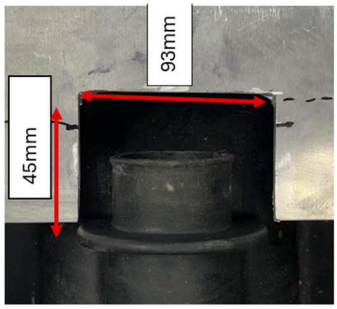	*A 45mm × 93mm rectangular cutout was introduced at the rear of the plate to provide clearance for the jet pump assembly.*	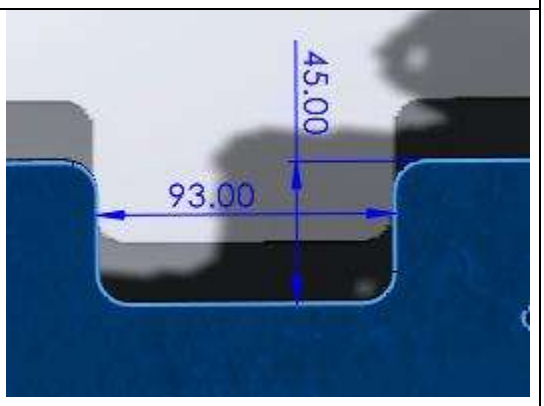
	*The hull mounting bolt hole pattern did not correspond to the hull bolt locations. The holes were repositioned to match the hull mounting pattern.*	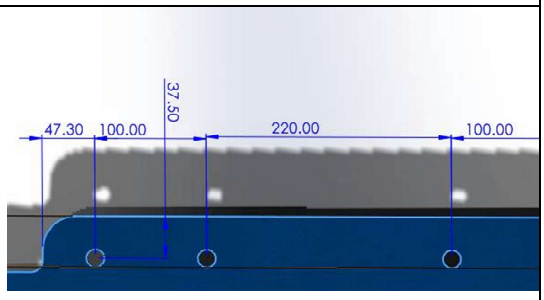

Appendix A4: Base plate loading derivations

Case 1:

Load Cases:

Load cases	**Location**
Pressure from battery mass	On the battery locations
Gravity force	Everywhere

Pressure from battery mass

$$\sigma_{batteries} = \frac{F_{Batteries}}{A_{Battery}} = \frac{m_{batteries}g}{A_{Battery}}$$

Where:

- $m_{batteries} = 11.6kg$
- $g = 9.81m/s^2$
- $A_{Battery} = 340mm \times 133mm = 4522mm^2 = 0.04522m^2$

$$\sigma_{batteries} = \frac{F_{Batteries}}{A_{Battery}} = \frac{(11.6)(9.81)}{0.04522} = 2516.5Pa$$

Case 2:

Load Cases:

Table A4.1: Case 2 loading parameters

Load cases	**Load type**	**Location**	**Symbol**	**Value**	**Source of Information**
Pressure from battery mass	Pressure	On the battery locations	$\sigma_{batteries}$	$2516.5Pa$	Derived
Weight of outboard motor and rear foil assembly less buoyancy	Vertical force	On the rear top plate centre	F_w	857N	Derived
Lift force from rear foil	Vertical Force	On the rear top plate centre	F_L	215N	Found from Will McAullay
Drag force from rear foil	Horizontal force	On the rear top plate centre	F_d	36N	Found from Will McAullay
Horizontal force from propulsion	Horizontal force	On the rear top plate centre	T	913N	Derived
Moment from rear foil weight	Moment	On the rear top plate centre	M_w	$164.99Nm$	Derived
Moment from rear foil lift force	Moment	On the rear top plate centre	M_L	$71.45Nm$	Derived
Moment from rear foil drag force	Moment	On the rear top plate centre	M_D	$45\ Nm$	Derived
Moment from Thrust	Moment	On the rear top plate centre	M_T	$1141Nm$	Derived

Final Resultant Forces/Moments	**Derivation**	**Value**
Vertical Force	$F_v = -F_w + F_L$	$-642.0N$
Horizontal Force	$F_H = -T + F_d$	$877.0N$
Total bending Moment	$M = M_T + M_w - M_L - M_D$	$1189.54Nm$
Front two bolts on rear plate	$F_{bolt,front} = \frac{M}{4d}$	2703.5N
Rear two bolts on rear plate	$F_{bolt,rear} = -\frac{M}{4d}$	-2703.5N
Total Vertical Force on front two bolts	$F_{v\ front,total} = F_v + F_{bolt,front}$	2061.5N

Total Vertical Force on rear two bolts	$F_{v\,rear,total} = F_v - F_{bolt,front}$	-3345.5N

At 25% of rear foil loading:

Table A4.2: Case 2 loading parameters at 25%

Final Resultant Forces/Moments	Derivation	Value	Applied Load (25% of Total)
Horizontal force	F_H	$877.0N$	$219.25N$
Total vertical force on front two bolts	$F_{v\,front,total}$	2061.5N	515.38N
Total vertical force on rear two bolts	$F_{v\,rear,total}$	-3345.5N	-836.38N

Weight of outboard motor and rear foil assembly:

$$F_w = W - F_{buoyancy}$$

$$F_w = W - \rho_{water} g V$$

Where;

- $\rho_{water} = 1000kg/m^3$
- $g = 9.81m/s^2$
- $V = 0.00981m^3$- found from CAD model

$$F_w = 953.24N - (1000)(9.81)(0.00981)$$

$$F_w = 857N$$

Horizontal force from propulsion

Assuming cruise speed is at 50% efficiency:

$$T = \frac{P}{v}$$

Where:

- Thruster power is 18.8kW, 50% efficiency is 9.4kW
- Maximum velocity is 10.29m/s (20knots)

$$T = \frac{9.4 \times 10^3}{10.29 m/s} = 913N$$

Moment from rear foil weight

$$M_w = r_{COM} F_w$$

Where:

- r is the distance from point of attachment to the centre of mass of the foil assembly, this value is 0.19252m
- $F_w = 857N$

$$M_w = 0.19252 * 857N = 164.99Nm$$

Moment from rear foil lift force

$$M_L = r_{COL} F_L$$

Where:

- r is the distance from point of attachment to the centre of lift from the foil, this value is 0.33234m
- $F_L = 215N$

$$M_L = 0.33234 * 215N = 71.45Nm$$

Moment from rear foil drag force

$$M_D = r_{COD} F_d$$

Where:

- r is the distance from point of attachment to the centre of drag from the foil, this value is 1.25m
- $F_d = 36N$

$$M_L = 1.25 * 36N = 45Nm$$

Moment from Thrust

$$M_P = r_{COT}T$$

Where:

- r is the distance from point of attachment to the centre of propulsion from the foil, this value is assumed to be the same as the centre of drag at 1.25m
- $T = 913N$

$$M_P = 1.25m * 913N = 1141Nm$$

Calculating force per Bolts:

Assuming the rear foil is attached to the rear base plate via a plate with 4 bolts at each end corner of the plate. The resultant moment generated will transfer a force into the front two bolts, the magnitude of this force is:

$$M = 4F_{bolt,i}d$$

$$F_{bolt,front} = \frac{M}{4d}$$

Where $d = 0.11m$

Equally, the rear two bolt will experience the same force in the negative direction, this is displayed as:

$$F_{bolt,rear} = -\frac{M}{4d}$$

Load Case 3 – From foil loading cases

The front foil will generate a lift force equal to the weight of the jet ski, including the front foil and rear foil, less the lift force generated from the rear foil, the worst case scenario will be the instance the jetski is rising as the craft is accelerating upwards, and the force is modelled as

$$\sum F_z = ma$$

$$F_{L,front} + F_{L,rear} - W_{jetski} = ma$$

Acceleration of the craft is maximum of 1 m/s^2

$$F_{L,front} = W_{jetski} - F_{L,rear} + ma$$

$$F_{L,front} = 250kg * 9.81 - 215N + 250 * 1$$

$$F_{L,front} = 2487.5N$$

Assuming the lift force is distributed amongst the 8 bolt washers, the force per bolt is:

$$F_{i\,L,} = \frac{2487.5N}{8} = 310.94N$$

To estimate the drag force, the lift to drag ratio assumed to be consistent across both the front and rear foil, as the foil profile was the same, the rear foil had experienced a lift to drag ratio of 5.97:

$$L{:}\,D = \frac{215}{36} = 5.97$$

Therefore, the drag force experienced by the front foil will be:

$$F_{D,front} = \frac{2487.5N}{5.97} = 416.67N$$

The drag force will be distributed equally amongst the bolts, and are therefore:

$$F_{i\,D,front} = 52.08N$$

This drag force will be transmitted as both a moment acting on the bolts and a horizontal force on the bolts, as the bolt structure consists of 4 bolts on a row on either side of the clearance aperture. The bolts on the outer end will experience a greater force from this moment, the horizontal force will be equal amongst the bolts. The moment generated by the front foil drag is:

$$M_{front} = F_{D,front} r$$

Where r is the distance from the point of drag to the base plate, this distance is approximately 1075mm.

$$M_{front} = 416.67N * 1.075m$$

$$M_{front} = 447.92Nm$$

The translated force into the washer at each bolt hole is defined by table X. and is defined by

$$F_i = \frac{Mr_i}{\sum r^2}$$

Table A4.3: Case 3 loading parameters at bolt locations

Bolt location	Distance from centroid, r_i	Force per bolt from moment, F_i
Rear far	90mm	1120N
Rear close	30mm	373N
Front close	30mm	-373N
Front far	90mm	1120N

The total vertical force at each bolt hole transmitted via the bolt washer is is defined by table X. The total vertical force per bolt is defined as:

$$F_{i,Total\ veritcal} = F_{i,M} + F_{i,L}$$

Table A4.4: Case 3 loading parameters at bolt locations final forces

Bolt location	Force per bolt from moment, $F_{i,M}$	Force per bolt from lift force, $F_{i,L}$	Total Vertical force per bolt $F_{i,Total\ veritcal}$
Rear far	1120N	310N	1430N
Rear close	373N	310N	683N
Front close	-373N	310N	-63N
Front far	-1120N	310N	-810N

Appendix B1: Waterproofing Case Drawings

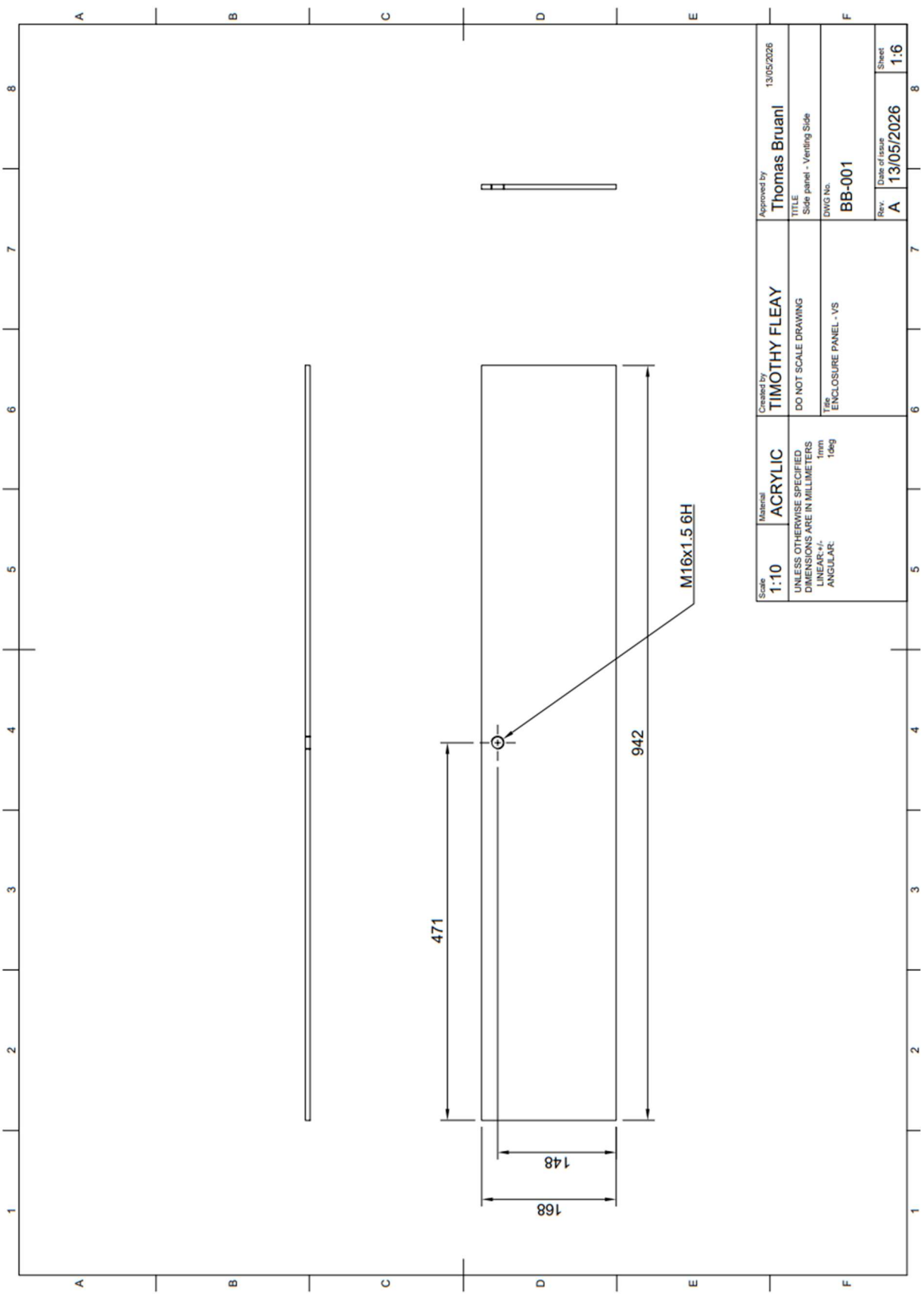

Figure B1.1: BB-001 Drawings

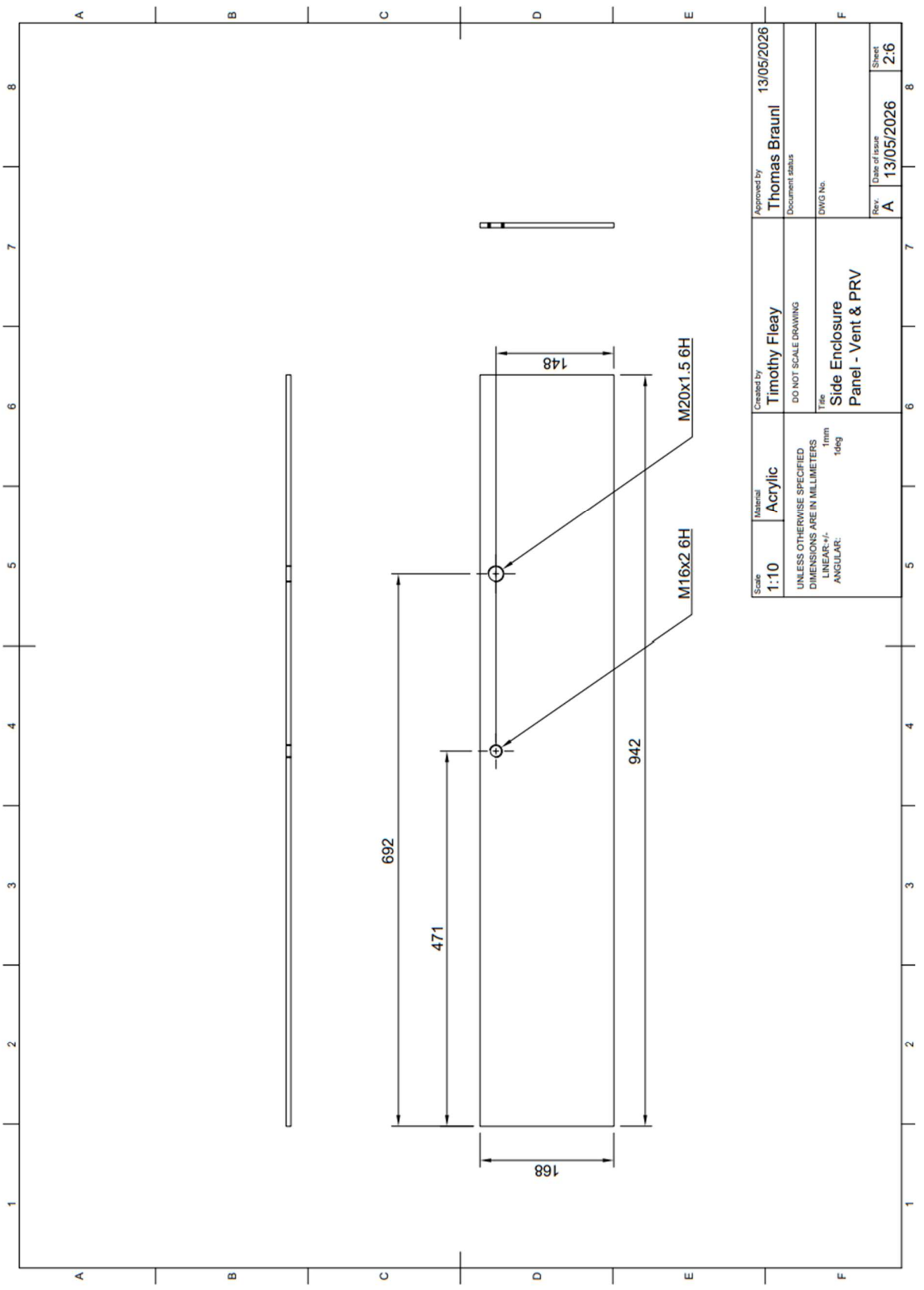

Figure B1.2: BB-002 Drawings

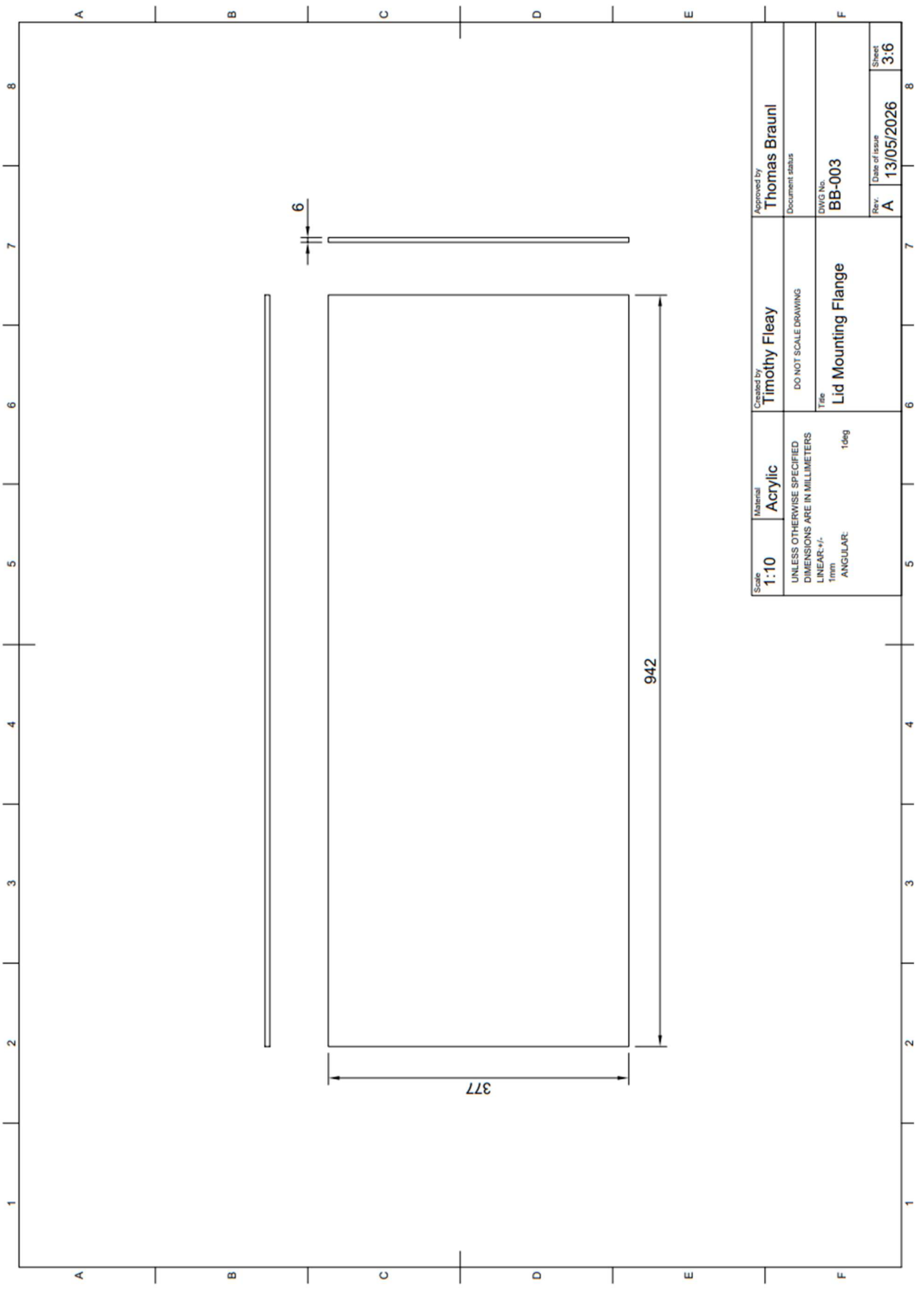

Figure B1.3: BB-003 Drawings

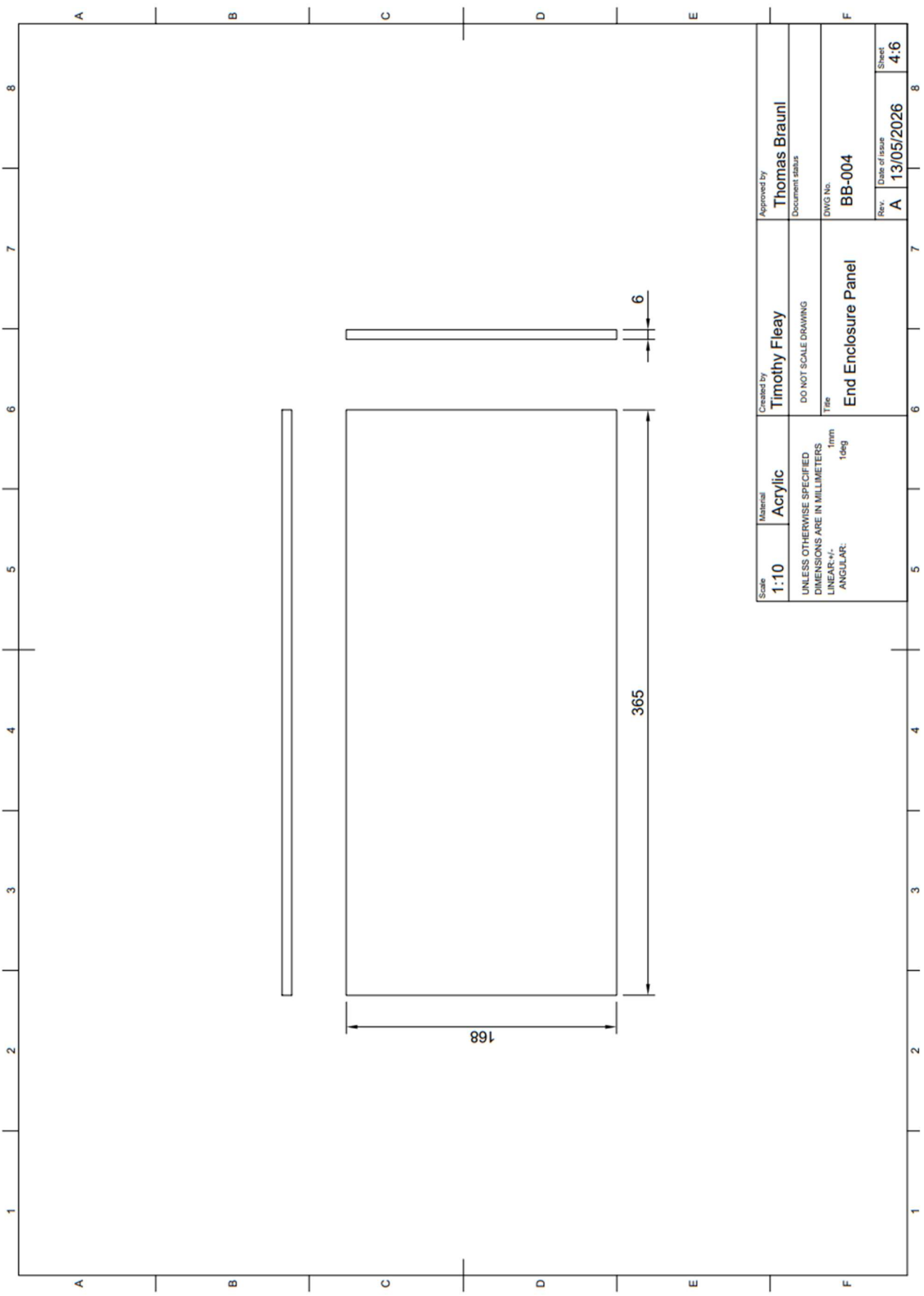

Figure B1.4: BB-004 Drawings

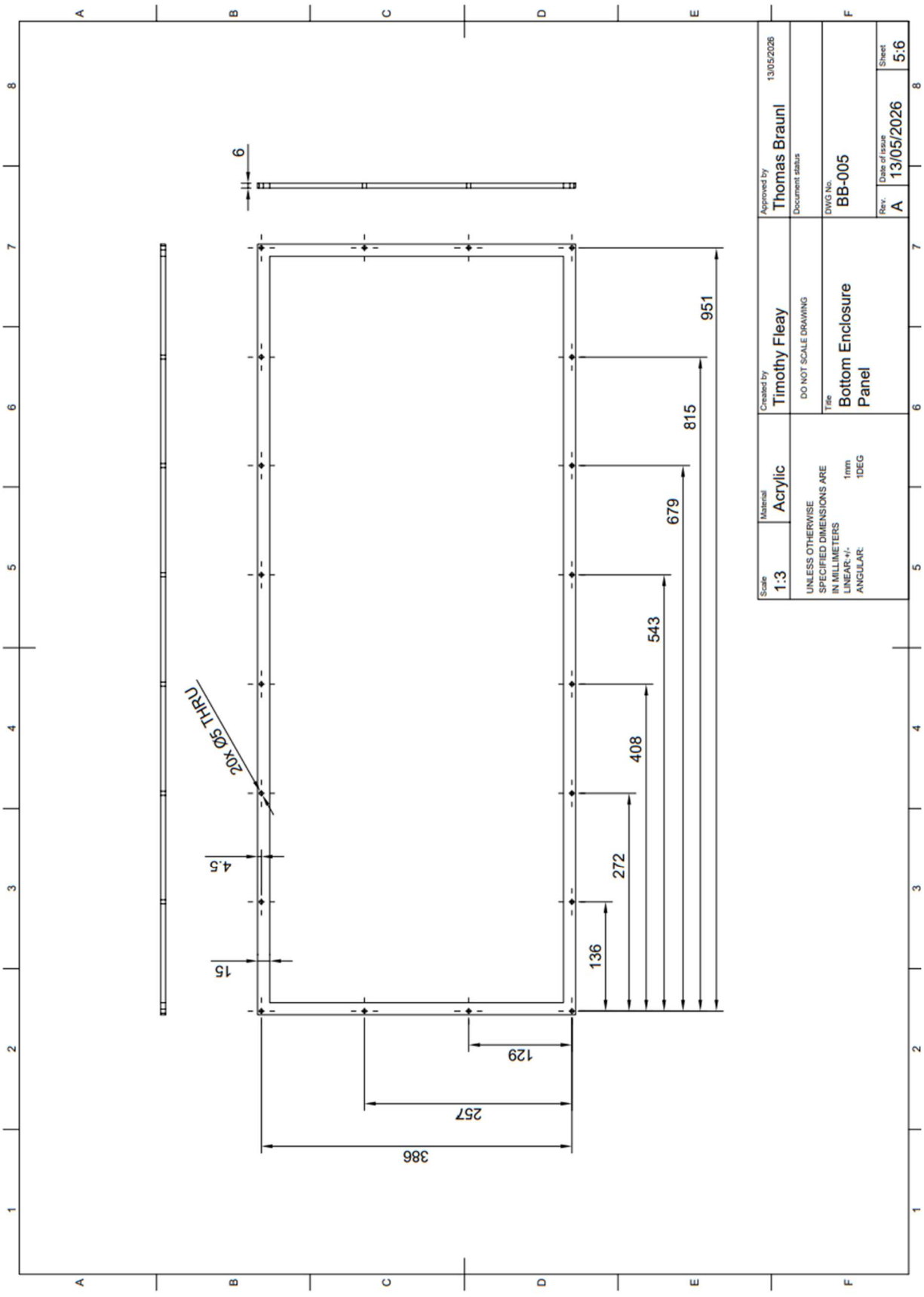

Figure B1.5: BB-005 Drawings

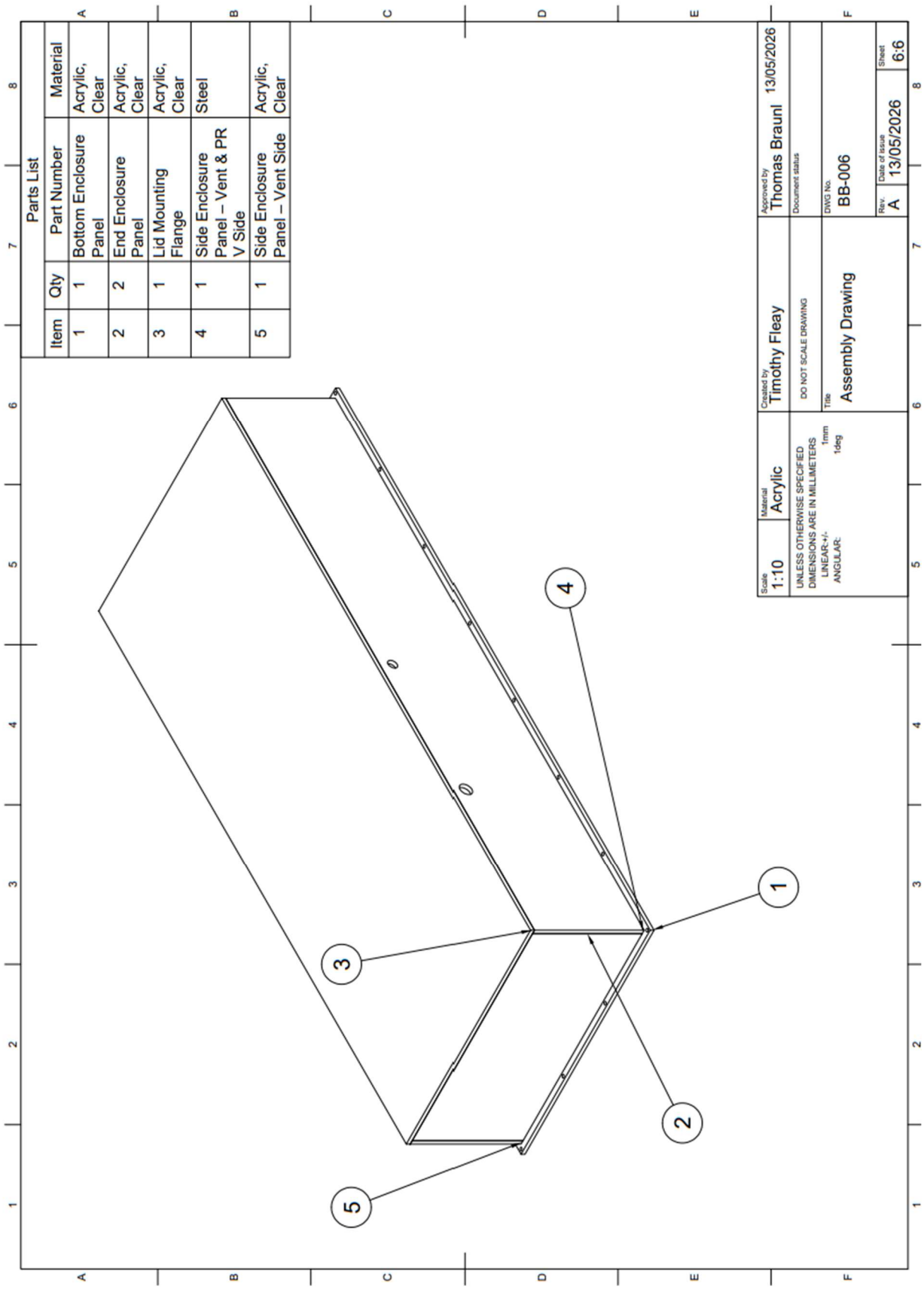

Figure B1.6: BB-006 Drawings

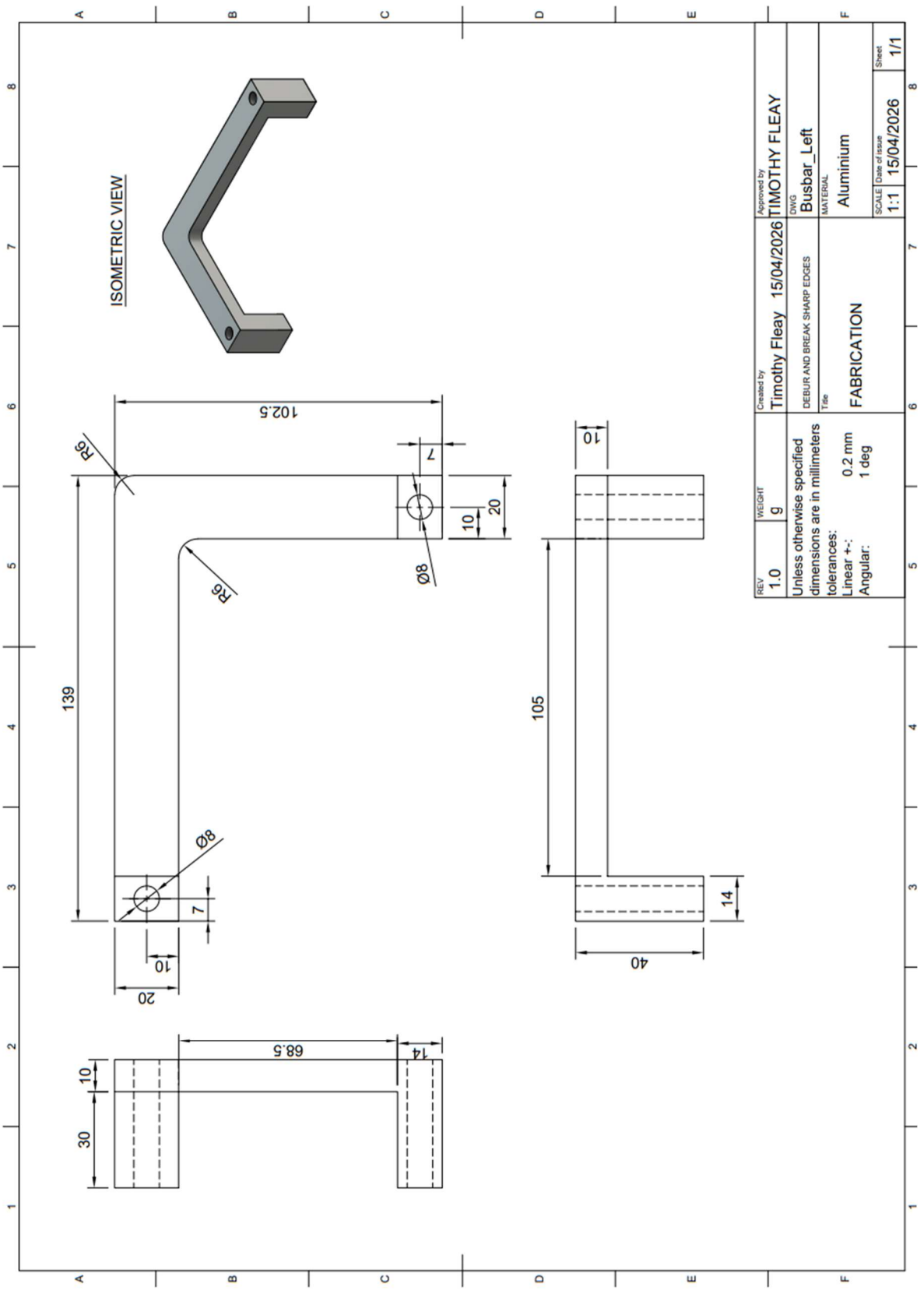

Figure B2.1: Left busbar refabrication Drawings

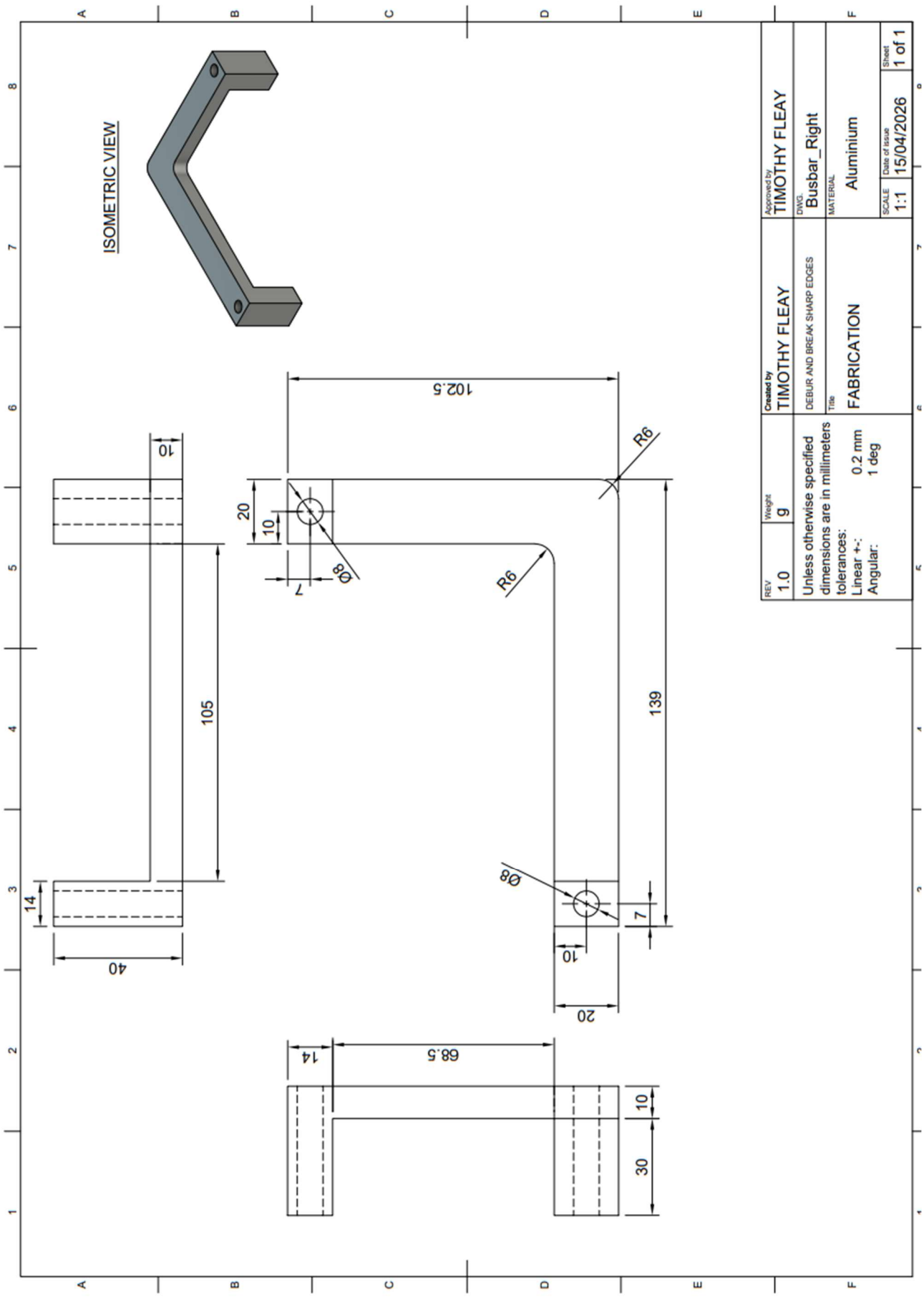

Figure B2.2: Right busbar refabrication Drawings

Appendix B2: Acrylic Case, busbar and pressure valve cost summary and part tables

Table B2.1: Acrylic case cost table

Cost Item	Cost per Unit	Quantity	Subtotal ($AUD)
Raw Stock Material Cost			
Acrylic Panels	$100	2	$200
EPDM Roll - Bunnings	$23	3m	$23
Pressure Relieve Valve	$27.50	1	$27.50
Breather Valves	$23.40	2	$46.80
Aluminum block	$30	2	$60
Total Raw Material Cost			**$357.30**
Fabrication and Assembly Costs			
Aluminum Busbar Manufacture Service	$100		$100
Acrylic Enclosure Manufacture Service	$220		$220
Total Fabrication and Assembly Cost			**$320**
Total Manufacturing Costs			**$677.30**

Table B2.2: Breather vent part table

Component: Breather Vent	**JDAE12PA/SW - Aliexpress**
Size	M12 x 1.5
Air Flow (mL/min/cm^2)	90-130
Protection Grade	IP69
Water entry pressure (bar)	> 1 b
Minimum air flow pressure (bar)	0.01
Membrane	Polyether Sulphone

Table B2.3: Pressure relief valve part table

Component: *Pressure Relief Valve*		**VENT-MS4NME-O8002 – Amphenol LTW**
Size	M20 x 1.5	
Air Flow (mL/min)	>1400ml/min	
Protection Grade	IP68	
Water entry pressure (kPa/60s)	> 60	
Min air flow pressure (bar)	7kPa	
Opening Pressure (kPa)	12 ± 2	

Table B2.4: EPDM part table

Component: *Moroday EPDM rubber*		**Bunnings**
Size	50mm x 3mm x 3m	
Material	EPDM	
Protection Grade	IP68	
Water entry pressure (kPa/60s)	> 60	
Min air flow pressure (bar)	7kPa	
Opening Pressure (kPa)	12 ± 2	

Table B2.5: case bolts part table

Component: *Pinnacle M4 x 25mm Zinc Plated Hex Head Bolts and Nuts Pack of 8*		**Bunnings**
Size	M4 x 25mm	
Material	Steel	
Quantity	3 packs	
Thread pitch	0.7mm	

Appendix B3: Relief Valve Flow Rate Analysis

The enclosure consists of five acrylic faces, and one aluminium base plate on which the battery cells sit. Each wall material is modelled as a separate thermal node, reflecting their different thermal masses and external convective conductance's

The enclosure is modelled as four lumped thermal nodes in series

- Battery (T_b): The battery pack is treated as a single lumped mass generating heat at a constant rate of $\dot{Q}_b$
- Internal air (T_a): The enclosed air recived heat from the batteries and loses heat to the acrylic wall by conection
- Acrylic Wall (T_w): The acrylic enclosure wall receives heat from the internal air and loses heat to the outside ambient by external convection
- Aluminium Base ($T_{w,al}$): Base plate on which batteries sit on

The four coupled energy balance equations are;

Battery:

$$m_b c_b \frac{dT_b}{dt} = \dot{Q}_b - h_{ba} A_b (T_b - T_a)$$

Where:

- m_b = battery mass
- c_b = battery specific heat capacity
- $\dot{Q}_b$ = battery heat generation
- h_{ba}= convection coefficient between battery and air
- A_b = battery surface area
- T_b = Temperature of battery as a function of time
- T_a = Temperature of air as a function of time

The battery heat stored = heat generated by battery − heat lost from battery to internal air

Internal air

$$m_a c_a \frac{dT_a}{dt} = h_{ba} A_b (T_b - T_a) - h_{aw} A_w (T_a - T_w) - h_{aw} A_{al} (T_a - T_{w.al})$$

Where:

- m_b = air mass
- c_b = air specific heat capacity
- h_{aw}= convection coefficient between air and wall
- A_w = acrylic wall surface area
- T_w = Temperature of wall as a function of time

Acrylic Wall:

$$m_{ac}c_{ac}\frac{dT_{w,ac}}{dt} = h_{aw}A_{ac}(T_a - T_{w,ac}) - h_{wo,ac}A_{ac}(T_{w,ac} - T_\infty)$$

Where:

- m_w = acrylic wall mass
- c_w = acrylic specific heat capacity
- h_{wo}= convection coefficient between wall and outside air
- A_w = acrylic wall surface area
- T_∞ = ambient air temperature (25℃)

Base plate:

$$m_{al}c_{al}\frac{dT_{w,al}}{dt} = h_{aw}A_{al}(T_a - T_{w,al}) - h_{wo}A_{al}(T_{w,al} - T_\infty)$$

Geometry and Air volume:

The enclosure dimensions are 940 mm × 340 mm × 170 mm, giving an internal volume of:

V_{enc}= 0.940 × 0.340 × 0.170 = 0.0543 m^3 = 54.3 L

Each battery cell has dimensions 355 mm × 151 mm × 108 mm. With five cells, the total battery volume is:

$V_{battery}$= 5 × (0.355 × 0.151 × 0.108) = 0.02895 m^3 = 28.95 L

The internal air volume available for expansion is therefore:

V_{air}= V_{enc} − $V_{battery}$ = 0.0543 − 0.02895 = 0.02535 m^3 = 25.4 L

The total internal wall surface area (sum of five faces) is:

A_{wall}= 2(0.340×0.170+ 0.940×0.170) + 0.940×0.340 = 0.7548 m^2

Thermal Masses:

Air:

$V_{air} = 0.02895m^3$, $\rho_{air} = 1.2kg/m^3$, $c_{p,a} = 1005J/(kg \cdot K)$

$m_aC_{p,a} = V_{air}\rho_{air}C_{p,a} = 0.02895m^3 \cdot 1.2kg/m^3 \cdot 1005J/(kg \cdot K)$

$$m_aC_{p,a} = 35J/K$$

Battery Pack

5 cells each weighing 11.6kg and an assumed specific heat capacity of 1,100J/kg·K:

$$m_bC_b = 5 \times 11.6 \times 1{,}100 = 63{,}800\,J/K$$

Acrylic wall

$(\rho = 1{,}180\,kg/m^3, Cp = 1{,}470\,J/kg \cdot K)$:

$m_{ac}C_{ac} = 1{,}180 \times (0.7548 \times 0.006) \times 1{,}470 = 7855.65\,J/K$

Aluminium base

$(\rho = 2{,}700\, kg/m^3, Cp = 900\, J/kg \cdot K)$:

$m_{al}C_{al} = 2{,}700 \times (0.3196 \times 0.003) \times 900 = 2{,}330\, J/K$

Convective Conductance's

The internal convection coefficient $h_{aw} = 5W/m^2 \cdot K$ applies to both internal wall surfaces (still enclosed air). The external coefficients differ by material

Internal air to acrylic inner face:

$$h_{aw} = 5W/m^2 \cdot K$$

Internal air to aluminium inner face:

$$h_{aw} = 5W/m^2 \cdot K$$

Outside acrylic wall to interior hull: $h_{wo,ac} = 10W/m^2 \cdot K$

Outside aluminium wall to internal hull: $h_{wo,ac} = 10W/m^2 \cdot K$

$$h_{aw}A_{ac} = 5.0 \times 0.7548 = 3.774\, W/K$$

$$h_{aw}A_{al} = 5.0 \times 0.3196 = 1.598\, W/K$$

$$h_{wo,ac}\, A_{ac} = 10.0 \times 0.7548 = 7.548\, W/K$$

$$h_{wo,al}\, A_{al} = 10.0 \times 0.3196 = 3.196\, W/K$$

The battery to internal air is follow is:

$$h_{ba,}A_b = 15.0 \times 1.0825\text{m}^2 = 16.24\, W/K$$

A summary of parameters is followed by

Table B3.1: Summary of key parameters

Parameter	Value	Description
$\dot{Q}_b$	$112.5\, W$	Battery heat generation
m_bC_b	$63{,}800\, J/K$	Battery thermal mass
$h_{ba,}A_b$	$16.24\, W/K$	Battery to internal air conductance
$m_aC_{p,a}$	$35\, J/K$	Internal air thermal mass

Parameter	Value	Description
V_{air}	$0.02895m^3$	Internal air volume
$m_{ac}C_{ac}$	$7855.65J/K$	Acrylic wall thermal mass (5 faces)
$m_{al}C_{al}$	$2{,}330\ J/K$	Aluminium base thermal mass (3 mm)
$h_{aw}A_{ac}$	$3.774\ W/K$	Air to acrylic wall conductance
$h_{aw}A_{al}$	$1.598\ W/K$	Air to aluminium base conductance
$h_{wo,ac}\ A_{ac}$	$3.196\ W/K$	Acrylic wall to ambient conductance
$h_{wo,al}\,A_{al}$	$7.990\ W/K$	Aluminium base to chassis conductance
T_∞	$25\ °C$	Ambient outside temperature

Ventilation Flow Rate Derivation

Ideal Gas Expansion

A constant pressure, the volume occupied by a fixed mass of air scales with absolute temperature (Charles's Law):

$$V(t) = Vair \times \frac{T_a(t)}{T_0}$$

Where T is in Kelvin. Differentiating with respect to time gives the volumetric flow rate of air displaced through the vent:

$$\dot{V}(t) = \left(\frac{V_{air}}{T_a}\right) \cdot \frac{dTa}{dt}$$

Substituting the energy balance for the air node:

$$\frac{dT_a}{dt} = \frac{h_{ba}A_b(T_b(t) - T_a(t)) - h_{aw}A_w(T_a(t) - T_w(t)) - h_{aw}A_{al}(T_a(t) - T_{w.al}(t))}{m_a c_a}$$

The full expression becomes:

$$\dot{V}(t) = \left(\frac{V_{air}}{T_a + 273.15}\right) \cdot \frac{h_{ba}A_b(T_b(t) - T_a(t)) - h_{aw}A_w(T_a(t) - T_w(t))h_{aw}A_{al}(T_a(t) - T_{w.al}(t))}{m_a c_a}$$

Numerical Solution:

The thermal behaviour of the four-node enclosure system is governed by four coupled first-order ODEs, one for each node (battery, internal air, acrylic wall, and aluminium base plate), which are integrated simultaneously using the fourth-order Runge-Kutta (RK4) method. At each time step of $\Delta t = 0.5$ s, RK4 evaluates the derivative vector four times — at the current state (k_1), two midpoint estimates (k_2, k_3), and a full-step estimate (k_4) — then advances the solution as a weighted combination in the ratio 1:2:2:1, achieving fourth-order accuracy without requiring the second- or higher-order derivatives that an analytical approach would demand. This makes it well-suited to the nonlinear coupling present here, where the air node temperature drives heat transfer to both wall nodes simultaneously. The integration was carried out over a 7200-second (two-hour) window, producing time histories for all four nodal temperatures and the derived ventilation flow rate, from which steady-state values and the peak outgassing rate were extracted.

The maximum volume flow rate is:

$$\dot{V}(t)_{max} = 7.80 mL/min \text{ @ } 6.4 \text{ minutes}$$

Python Code

```
4-Temperature Lumped Thermal Model — Battery Enclosure
=======================================================
Four coupled first-order ODEs solved
using the classical fourth-order Runge–Kutta (RK4) method.

Nodes:  Tb    = battery temperature          (°C)
        Ta    = internal air temperature     (°C)
        Tw_ac = acrylic wall temperature     (°C)  [5 faces]
        Tw_al = aluminium base plate temp    (°C)  [1 face]

Governing equations:
   mb*Cb   * dTb/dt   = Qdot
                      - hba*Ab*(Tb - Ta)

   ma*Ca   * dTa/dt   = hba*Ab*(Tb - Ta)
                      - haw*Aac*(Ta - Tw_ac)
                      - haw*Aal*(Ta - Tw_al)

   mac*Cac  * dTw_ac/dt = haw*Aac*(Ta - Tw_ac)
                      - hwo_ac*Aac*(Tw_ac - T_inf)

   mal*Cal  * dTw_al/dt = haw*Aal*(Ta - Tw_al)
                      - hwo_al*Aal*(Tw_al - T_inf)

Ventilation flow rate (ideal gas, constant pressure):
   Vdot(t) = (V_air / (Ta + 273.15)) * dTa/dt
"""

import numpy as np
```

```
import matplotlib.pyplot as plt

# ------------------------------------------------------------------------
# Parameters (updated from refined parameter table)
# ------------------------------------------------------------------------

# Heat source and boundary condition
Qdot   = 112.5     # W     battery heat generation (I²R, I=75A, R=0.02Ω)
T_inf  = 25.0      # °C    ambient outside temperature
T0     = 25.0      # °C    initial temperature (all nodes)

# Battery thermal mass and conductance
mb_Cb  = 63_800    # J/K   battery thermal mass
hba_Ab = 16.24     # W/K   battery to internal air conductance

# Internal air
ma_Ca  = 35.0      # J/K   internal air thermal mass (refined)
V_air  = 0.02895   # m³    internal air volume (refined)

# Wall thermal masses
mw_Cw_ac = 7855.65  # J/K   acrylic wall thermal mass, 5 faces (refined)
mw_Cw_al = 2_330.0  # J/K   aluminium base thermal mass, 3 mm

# Conductances
haw_Aw_ac = 3.774   # W/K   air to acrylic wall conductance
haw_Aw_al = 1.598   # W/K   air to aluminium base conductance
hwo_Ao_ac = 7.548   # W/K   acrylic wall to ambient conductance
hwo_Ao_al = 7.990   # W/K   aluminium base to chassis conductance

# ------------------------------------------------------------------------
```

```
# ODE right-hand side
# ----------------------------------------------------------------------

def derivatives(state):
    """
    Returns [dTb/dt, dTa/dt, dTw_ac/dt, dTw_al/dt].
    state = [Tb, Ta, Tw_ac, Tw_al]  all in °C.
    """
    Tb, Ta, Tw_ac, Tw_al = state

    dTb    = (Qdot - hba_Ab * (Tb - Ta)) / mb_Cb

    dTa    = (  hba_Ab    * (Tb - Ta)
            - haw_Aw_ac * (Ta - Tw_ac)
            - haw_Aw_al * (Ta - Tw_al)) / ma_Ca

    dTw_ac = (haw_Aw_ac * (Ta - Tw_ac)
            - hwo_Ao_ac * (Tw_ac - T_inf)) / mw_Cw_ac

    dTw_al = (haw_Aw_al * (Ta - Tw_al)
            - hwo_Ao_al * (Tw_al - T_inf)) / mw_Cw_al

    return np.array([dTb, dTa, dTw_ac, dTw_al])

# ----------------------------------------------------------------------
# RK4 integrator
# ----------------------------------------------------------------------

def rk4_step(state, dt):
    """Single classical RK4 step."""
```

```
    k1 = derivatives(state)
    k2 = derivatives(state + 0.5 * dt * k1)
    k3 = derivatives(state + 0.5 * dt * k2)
    k4 = derivatives(state + dt * k3)
    return state + (dt / 6.0) * (k1 + 2*k2 + 2*k3 + k4)

def solve(t_end=7200.0, dt=0.5):
    """
    Integrate the 4-node system from t=0 to t=t_end using RK4.

    Returns
    -------
    t     : time array (s)
    Tb    : battery temperature (°C)
    Ta    : internal air temperature (°C)
    Tw_ac : acrylic wall temperature (°C)
    Tw_al : aluminium base temperature (°C)
    Vdot  : ventilation flow rate (mL/min)
    """
    n = int(t_end / dt)
    t    = np.zeros(n + 1)
    Tb   = np.zeros(n + 1)
    Ta   = np.zeros(n + 1)
    Tw_ac = np.zeros(n + 1)
    Tw_al = np.zeros(n + 1)
    Vdot  = np.zeros(n + 1)

    state = np.array([T0, T0, T0, T0])
    Tb[0], Ta[0], Tw_ac[0], Tw_al[0] = state
```

```
    for i in range(n):
        state     = rk4_step(state, dt)
        t[i+1]    = (i + 1) * dt
        Tb[i+1]   = state[0]
        Ta[i+1]   = state[1]
        Tw_ac[i+1] = state[2]
        Tw_al[i+1] = state[3]

        dTa_dt    = derivatives(state)[1]
        Ta_K      = state[1] + 273.15
        Vdot[i+1]  = (V_air / Ta_K) * dTa_dt * 1e6 * 60   # mL/min

    return t, Tb, Ta, Tw_ac, Tw_al, Vdot

# ---------------------------------------------------------------------------
# Run and report
# ---------------------------------------------------------------------------

t, Tb, Ta, Tw_ac, Tw_al, Vdot = solve(t_end=7200.0, dt=0.5)

peak_idx  = np.argmax(Vdot)
peak_flow = Vdot[peak_idx]
peak_time = t[peak_idx]

print("=" * 58)
print("  4-Node Thermal Model Results  (with aluminium base)")
print("=" * 58)
print(f"  Peak ventilation rate : {peak_flow:.4f} mL/min")
print(f"                          {peak_flow/60000:.4e} L/s")
print(f"  Time of peak          : {peak_time:.1f} s  ({peak_time/60:.1f} min)")
```

```
print(f"  Steady-state Tb      : {Tb[-1]:.2f} °C")
print(f"  Steady-state Ta      : {Ta[-1]:.2f} °C")
print(f"  Steady-state Tw_ac    : {Tw_ac[-1]:.2f} °C")
print(f"  Steady-state Tw_al    : {Tw_al[-1]:.2f} °C")
print("=" * 58)

# AS/NZS 3004.2:2014 compliance check
A_eff_cm2 = 133.5e-2       # cm²
qv_Ls     = peak_flow / 60_000
print(f"\nAS/NZS 3004.2:2014 check:")
print(f"  A_eff        = {A_eff_cm2:.4f} cm²")
print(f"  100 × qv      = {100 * qv_Ls:.5f} cm²")
print(f"  Standard met?  {'YES ✓' if A_eff_cm2 > 100 * qv_Ls else 'NO ✗'}")

# ---------------------------------------------------------------------------
# Plots
# ---------------------------------------------------------------------------

fig, (ax1, ax2) = plt.subplots(2, 1, figsize=(9, 7), sharex=True)
fig.suptitle("4-Node Lumped Thermal Model — Battery Enclosure\n"
          "(5-face acrylic + aluminium base plate)",
          fontsize=12, fontweight="bold")

t_min = t / 60

ax1.plot(t_min, Tb,    color="#E24B4A", lw=1.8, label="$T_b$ battery")
ax1.plot(t_min, Ta,    color="#378ADD", lw=1.8, label="$T_a$ internal air")
ax1.plot(t_min, Tw_ac, color="#1D9E75", lw=1.8, label="$T_{w,ac}$ acrylic wall")
ax1.plot(t_min, Tw_al, color="#7F77DD", lw=1.8, label="$T_{w,al}$ aluminium base",
       linestyle="--")
```

```
ax1.axhline(T_inf, color="gray", lw=0.8, linestyle=":", label="$T_\\infty$ ambient")
ax1.set_ylabel("Temperature (°C)")
ax1.legend(loc="center right", fontsize=9)
ax1.grid(True, alpha=0.3)

ax2.plot(t_min, Vdot, color="#BA7517", lw=1.8)
ax2.axvline(peak_time/60, color="#BA7517", lw=0.8, linestyle="--",
        label=f"Peak {peak_flow:.2f} mL/min at t={peak_time/60:.1f} min")
ax2.set_xlabel("Time (min)")
ax2.set_ylabel("$\\dot{V}$ (mL/min)")
ax2.legend(fontsize=9)
ax2.grid(True, alpha=0.3)

plt.tight_layout()
plt.savefig("thermal_model_4node_results.png", dpi=150)
plt.show()
```

Appendix C1: Cost table and part tables

Table C1.1: Cost table for watercooling system

Cost Item	Cost per unit	Quantity	Total cost	Shipping cost	GST	Subtotal ($AUD)
	Raw Stock Material Cost					
ESC Cooling System						
Radiator Water Cooler	$25.09	1	$25.09	Free	$2.51	$27.60
Water Pump for PC	$36.56	1	$36.56	Free	$3.66	$40.22
Water cooling reservoir	$22.40	1	$22.40	Free	$2.24	$24.65
6mm x G1/4 male barb connectors	$0.19	6	$1.14	$9.57	$1.07	$11.78
PVC Flexible Pipe (5mm)	$19	-	$19	-	$1.4	$15.4
Motor Cooling System						
PVC Flexible Pipe (10mm)	$4.50/m	2m	$9.00	-	$0.90	$9.9
Sea Strainer	$6.23	1	$6.23	Free	$0.62	$6.85
Total Cost						**$136.40**

Table C1.2: Water reservoir parts table

Component: Water Cooling Reservoir	Aliexpress
Capacity (ml)	270
Thread Fitting Size	G1/4 BSP
Body Material	PMMA Plastic
Shell Material	POM High Temperature Resistant Rubber
Weight (g)	352

Table C1.3: Radiator parts table

Component: 10 Pipe High Performance Radiator Water Cooler		Bunnings
Size	157mm x 120mm x 32mm	
Thread Fitting Size	G1/4 BSP	
Material	Brass	
Pipe Diameter (mm)	8	
Number of Flat Tubes (pcs)	10	

Table C1.4: Water pump parts table

Component: 12V pump		Bunnings
Size	75mm x 61mm x 33mm	
Thread Fitting Size	G1/4 BSP	
Pressure Head (m)	3.5	
Maximum Flow (L/h)	500	
Voltage (V)	DC12	

Table C1.5: Pipe fitting connector parts table

Component: 6 x ¼" 6mm Brass Pipe Fitting Connectors		Bunnings
Connection	Male	
Type	TEE	
Pressure	<850kPa	
Material	Brass	

Table C1.6: PVC pipe parts table (5mm)

Component: PVC Clear Vinyl Tube Low Pressure Hose (5mm)		**Bunnings**
Size (mm)	5	
Length (m)	5	
Material	PVC	
Temperature range (°C)	-0 to +50	

Table C1.7: PVC pipe parts table (10mm)

Component: PVC Clear Vinyl Tube Low Pressure Hose (10mm)		**Clark Rubber**
Size (mm)	10	
Length (m)	2m	
Material	PVC	
Temperature range (°C)	-0 to +50	

Table C1.8: Steel pipe filter part table

Component: Stainless steel pipe filter		**Aliexpress**
Barb Size (mm)	10	
Material	Steel	
Maximum Pressure rating	<850kPa	

Appendix C2: Cooling flow-rate calculation

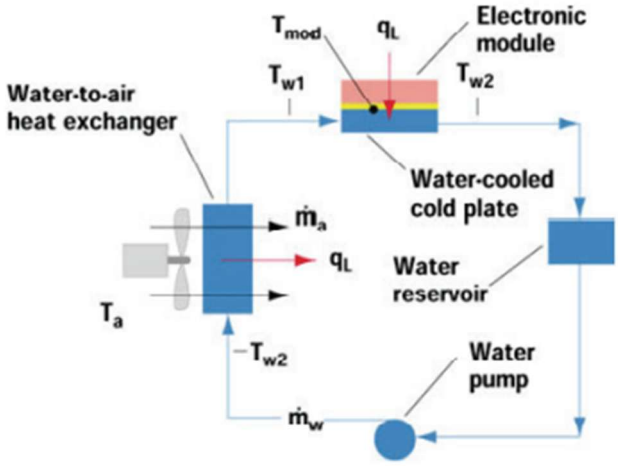

Table C2.1: Water-to-air heat exchanger diagram

The paper states that coolant temperature rise across the cold is:

$$T_{w2} - T_{w1} = \frac{q_L}{C_w} \tag{C2.1}$$

Where $C_w = \dot{m}c_p$, this is the heat capacity rate of water

$$\dot{m} = \frac{q_L}{c_p(T_{w2} - T_{w1})} \tag{C2.2}$$

q_L is the power dissipated by the device and C_w as the heat capacity rate of water, found from mass flow rate multiplied by the specific heat of water

For the ESC, the working amperage with water cooling is specified at 400A, with 85V:

$$P = VI = 85V \times 400A = 34{,}000W$$

It's unsure what efficiency the ESC runs at although range is from 95% to over 99%, meaning they won't dissipate too much heat, assuming a 98% efficiency [INSERT REFERNCE].

$$q_L = P(1 - \eta) \tag{C2.3}$$

$$q_L = 34000(1 - 0.98) = 680W$$

The temperature of the ESC is derived as:

$$T_{ESC} = q_L R_{cp} + T_{w1} \quad \text{(C2.4)}$$

Where:

- q_L is power dissipated by ESC
- R_{cp} is thermal resistance of the cold plate
- T_{w1} is the water temperature entering the cold plate

For the motor cooling system, the T_{w1} is predicable to being the temperature of the water, in the swan river, this value reaches 23°C to 26°C in summer, and 13°C to 16°C in winter

For the ESC cooling system, T_{w1} calculations are more difficult as there is a closed looped system, water temperature is both rising from power transferred from the ESC and dropping while its being transferring heat to the ambient in the heat exchanger.

Water temperature increase from ESC power dissipation is given by:

$$T_{w2} - T_{w1} = \frac{q_L}{C_w} \quad \text{(C2.5)}$$

- T_{w2} = temperature of water leaving the ESC and entering heat exchanger.
- C_w = heat capacity rate of water, where $C_w = \dot{m} c_p$

Once liquid enters the heat exchanger it transfers heat into the air. The amount of heat transferred at steady state is equal to the heat produced by the component.

$$q_L = \varepsilon C_{min}(T_{w2} - T_a) \quad \text{(C2.6)}$$

- T_a = Temperature of air entering the heat exchanger
- ε = effectiveness of the heat exchanger
- C_{min} = heat capacity rate of water C_w or C_a, whatever is smaller

Solving equations 1 and 4 to solve T_{ESC} gives:

$$T_{ESC} = q_L \left(R_{cp} + \left(\frac{1}{\varepsilon C_{min}} - \frac{1}{C_W} \right) \right) + T_a \quad \text{(C2.7)}$$

Several factors must be known to effectively use this equation.

First is the ESC cold plates thermal resistance, typically a cold plates design is driven by these limits, which control the minimum width of its internal channels and fins. A cold plates thermal resistance is usually in the range of 0.025 to 0.075°C/W, this depends on its size and material. Taking the midpoint of 0.05°C/W.

The heat exchanger performance is the product of its efficiency and the total specific capacity rate flowing through it (εC_{min}) this performance specifies the amount of heat removed from the heat exchanger at a given difference between the water and air temperatures

$$T_{ESC} = q_L\left(R_{cp} + \left(\frac{1}{\varepsilon C_{min}} - \frac{1}{C_w}\right)\right) + T_a$$

$q_L = 680W$

$R_{cp} = 0.05°\text{C/W}$

$\varepsilon = 0.5$

$T_a = 25°\text{C}$

Calculating the heat capacity rate of water:

$$C_w = \dot{m}c_p = 0.03833kg/s \cdot 4184$$

$$C_w = 160.37W/K$$

Calculating the heat capacity rate of air

$C_a = \dot{m}c_a = \varphi\rho A sin\theta v_{inflow} c_a$

- ρ is air density $= 1.225kg/m^3$
- θ is the angle of the radiator to the inflow of air $= 45°$
- A is the radiator dimensions $= 157\text{mm x } 120\text{mm} = 0.01884m^2$

The effective area of the radiator depends on the radiator open-area, roughly 30% of blockage comes from the radiator tubes, fins and frames, this comes from the manufacturer specifications reducing the area to:

$A_{eff} = 0.7A = 0.0131882m^2$

- v is the relative air velocity, this will be the velocity of the jet ski $= 5.144m/s$
- $c_a = 1005J/kgK$

$C_a = \varphi\rho A sin\theta v_{inflow} c_a$

$$C_a = (0.7)(1.225)A(sin45)(5.144)(1005)$$

$$C_a = 3134.63A$$

$C_{min} = \min(C_w, C_a) = \min(160.37, 3134.63A)$
Assuming $C_a < C_w$*:*

$$3134.63A < 160.22$$

$$A < 0.0511m^2$$

$$T_{ESC} = \begin{cases} 680\left(0.05 + \left(\frac{1}{3134.63A} - \frac{1}{160.37}\right)\right) + 25, & \text{A} \leq 0.0511\text{m}^2 \\ 59℃, & A > 0.0511\text{m}^2 \end{cases}$$

$$T_{ESC} = \begin{cases} 54.76 + \frac{0.2170}{A}, & \text{A} \leq 0.0511\text{m}^2 \\ 59℃, & A > 0.0511\text{m}^2 \end{cases}$$

The radiator area and jet ski speed have the greatest effect on the cooling capacity of the system. C_a is the

Pump flow rate estimation:

Using the Darcy-Weisbach equation, the pump head available can be estimated:

$$h_f = f\frac{L}{D}\frac{V^2}{2g} \tag{C2.8}$$

Where:

- L is the length of tube (2m)
- D is the diameter of the tube (0.005m)
- V is the velocity of the flow ($V = Q/A$)
- g is the gravity constant

f is the friction factor, for high Reynolds number, the friction factor can be predicted using the Swamee-Jain Equation:

$$f = \frac{0.25}{[\log_{10}(\frac{\frac{\varepsilon}{D}}{3.7} + \frac{5.74}{R_e^{0.9}})]\text{^}2} \tag{C2.9}$$

Where:

- ε is the absolute roughness of PVC, estimated to be 1.5×10^{-6}m

The Reynolds number is estimated as:

$$R_e = \frac{\rho V D}{\mu} \tag{C2.10}$$

Where:

- ρ is water density (1000kg/m^3)
- μ is the dynamic viscosity of water ($1.0 \times 10^{-3} Pa \cdot s$)

An iterative process was used to find the operating flow rate as the Q where:

$$H_{pump} = h_f \tag{C2.11}$$

This is the point where the pump head available = system head loss, the approximate pump curve modelled as linear is given as:

$$H_{pump} = H_{max}\left(1 - \frac{Q}{Q_{max}}\right) \tag{C2.12}$$

- H_{max} is given in the pump specification (3.5m)
- Q_{max} is given in the pump specification (8.33L/min)

Therefore:

$$H_{max}\left(1 - \frac{Q}{Q_{max}}\right) = f\frac{L}{D}\frac{V^2}{2g}$$

Using parameters define, an iterative process gives the following results:

Table C2.1: Iterative table to find operating flow rate

Q (L/min)	V (m/s)	Re	f	Pipe head loss h_f (m)	Pump Head (m)

2.0	1.70	8488	0.0329	1.93	2.66
2.2	1.87	9337	0.0321	2.28	2.58
2.3	1.95	9762	0.0317	2.46	2.53
2.35	1.99	9974	0.0315	2.56	2.51
2.4	2.04	10186	0.0313	2.65	2.49

The operating point is roughly:

$Q_{operaitng} = 2.33 L/min$

Table C2.2: List of parameters and respective assumptions

Parameter	Assumption	Justification
ESC efficiency	98%	Based on literature values for high-power DC motor ESC efficiency (Seymour, 2020)
ESC heat load, q_L	680 W (2% of 34 kW peak power)	Remaining power not converted to mechanical output is dissipated as heat (Seymour, 2020)
Cold plate thermal resistance, R_{cp}	0.05 °C/W	Midrange of the typical range 0.025 to 0.075°C/W for aluminium cold (Simons, 2002)
Heat exchanger effectiveness, ε	0.5	Conservative mid-range estimate for a single-pass crossflow heat exchanger under ram airflow, consistent with values reported in Kays & London (1984) (Kays & London, 1964)
Coolant	Water	High specific heat capacity and common use in compact closed-loop cooling circuits
Specific heat capacity of water, c_p	4180 J/kg·K	Standard value for liquid water at 25°C (Engineering Toolbox, 2024a)
Specific heat capacity of air, C_a	1005 J/kg·K	Standard value for dry air at 25°C (Engineering Toolbox, 2024b)
Air density, ρ	1.225 kg/m³	Standard atmospheric density at sea level and 25°C (Engineering Toolbox, 2024b)
Fin blockage factor, φ	0.7	Sourced from radiator manufacturer specification; accounts for reduced open airflow area through radiator fins and tubes
Radiator frontal area, A	0.01884 m²	Measured from selected radiator dimensions of 157 mm × 120 mm

Air velocity, v	5.144 m/s	Corresponds to vehicle speed of 10 knots — taken as the minimum foiling speed and conservative design point
Ambient air temperature, T_a	25°C	Representative ambient condition for outdoor marine operation
Hose length, L	2m	Estimated total length of PVC hose run between components in the closed-loop circuit
Hose internal diameter, D	0.005m	Inner diameter of selected 5mm PVC hose – This was measured
PVC absolute roughness, ε	1.5×10^{-6} m	Standard value for smooth PVC pipe surface roughness (Engineering Toolbox, 2024c)
Water dynamic viscosity, μ	1.0×10^{-3} Pa·s	Standard value for liquid water at 25°C — (Engineering Toolbox, 2024c)
Water density, ρ	1000 kg/m³	Standard value for liquid water at 25°C (Engineering Toolbox, 2024d)
Pump curve model	Linear model	Approximation of pump characteristic curve between rated maximum head and maximum flow; actual pump curve not published by manufacturer
Minor losses		Losses from bends, barb fittings, cold plate and radiator internal passages excluded due to undefined final system geometry; to be refined in future work